

1 **Insights into the petrogenesis of an intraplate**
2 **volcanic province: Sr-Nd-Pb-Hf isotope**
3 **geochemistry of the Bathymetrists Seamount**
4 **Province, eastern equatorial Atlantic**

5 Xiaojun Long¹, Froukje van der Zwan^{1,2,3}, Jörg Geldmacher¹, Kaj Hoernle^{1,2},
6 Folkmar Hauff¹, Dieter Garbe-Schönberg², Nico Augustin¹

7 ¹*GEOMAR Helmholtz Centre for Ocean Research Kiel, Wischhofstrasse 1-3, 24148 Kiel, Germany*

8 ²*Institute of Geosciences, Kiel University, Ludwig-Meyn-Strasse 10, 24118 Kiel, Germany*

9 ³*Present affiliation: King Abdullah University of Science and Technology (KAUST), Thuwal 23955, Saudi*
10 *Arabia*

11
12 **Abstract**

13 Unlike the well-studied narrow hotspot tracks, the origin of broadly distributed
14 seamount provinces remains a topic of conjecture. Here we present major and trace
15 element and **Sr-Nd-Hf-Pb** double spike isotope data of a comprehensive sample
16 suite from the Bathymetrists Seamount Province (a broad belt of submarine
17 volcanoes in the eastern equatorial Atlantic) and from the neighboring Cape Verde

Ridge (a topographic high on the shoulder of a local fracture zone). The major and trace element results are consistent with the Bathymetrists Seamount Province having formed in an intraplate setting. The isotopic composition of the seamount lavas resemble a HIMU-like signature ($^{206}\text{Pb}/^{204}\text{Pb}_{\text{in}} = 19.23\text{-}20.35$) similar, although not identical, to the nearby St. Helena hotspot composition. Based on plate tectonic reconstructions, a formation of the Bathymetrists Seamount Province by the postulated Sierra Leone plume, believed to be responsible for the geochemical anomaly at the mid ocean ridge at 1.7 °N and the nearby St. Peter and Pauls rocks, is not supported. An alternative model that the Bathymetrists Seamount Province was created by edge driven convection in the upper mantle along the boundary of the neighboring Sierra Leone Rise plateau is also not supported by the available data. Plate tectonic reconstructions, however, are consistent with a hotspot origin for the Bathymetrists Seamount Province, as is the presence of a seismic tomographic anomaly at the southwest end of the seamount belt.

1. Introduction

One of the most fundamental and at the same time most controversial debates in mantle dynamics and geochemistry within the last two decades centered on the

37 origin of intraplate volcanism. The characteristic incompatible-element and
38 radiogenic-isotope enriched composition of intraplate lavas (e.g. Hofmann and
39 Hart 1978; White 2010) have been generally attributed to deep mantle (plume)
40 sources that could have originated from as deep as the core-mantle boundary (e.g.,
41 Morgan, 1971, 1972a, b; Wilson, 1963). Opposing voices questioned this model
42 and argued that intraplate volcanism does not necessarily need to be associated
43 with a deep mantle plume, instead they propose that at least some intraplate
44 volcanism is derived from upper mantle or lithospheric processes by, e.g., small-
45 scale sub-lithosphere convection (King and Anderson, 1998; King and Ritsema
46 2000; Milelli et al., 2012; Ballmer et al., 2009; Reusch et al., 2010) or extension-
47 induced decompression melting (e.g., Foulger et al., 2005; Hieronymus and
48 Bercovici, 2000; Koppers et al., 2003; McDougall, 1971; Natland and Winterer,
49 2005; Sleep, 1984; Geldmacher et al., 2008) above chemically enriched zones in
50 the upper mantle. On the other hand, the original plume model has been
51 extensively enhanced by many authors over the last 60 years to accommodate new
52 observations of intraplate volcanism. In particular various combinations of plume
53 and (shallow) non-plume (primarily tectonic) processes have been proposed to
54 explain, e.g., the nonlinearity of hotspot tracks (e.g. Geldmacher et al., 2005;
55 Hoernle et al. 2016), the formation of isolated seamount volcanism by diffuse,
56 large-scale, lower-mantle (plume) upwellings (Niu et al., 2002; Waters, et al., 2011;

Long et al., in review), or the formation of seamount provinces or large igneous provinces at or near spreading centers (Hoernle et al., 2011a; Sager et al., 2019; Whittaker et al., 2015).

A further intraplate volcanic province which could have been generated as a result of such hybrid processes could be the Bathymetrists Seamount Province (BSP) in the Sierra Leone Basin in the equatorial Atlantic (Jones et al., 1991; Peyve and Skolotnev, 2009; Skolotnev et al., 2010; Skolotnev et al., 2017, Figure 1). The morphology of the irregular-shaped seamounts and elongated ridges of the BSP may reflect a prominent role for shallow, lithospheric control on magma formation and/or ascent through the crust possibly related to a prevailing tectonic fabric or to localized extension (van der Zwan et al., 2018). As the northern part of the BSP is located over multiple fracture zones/and or transform faults (Figure 1), it has been advocated that this orientation reflects a formation of the BSP by shallow processes (Jones, 1987; Jones et al., 1991; Skolotnev et al., 2010; 2012). The Sierra Leone Rise plateau borders the BSP to the southeast and shares its overall NE-SW oriented strike, similar to the orientation of hotspot tracks like St. Helena and Walvis Ridge in the South Atlantic and Cape Verde (southern islands) and Canary Islands in the North Atlantic. A mantle plume origin has been demonstrated and is generally accepted for each of these four hotspot tracks (Burke and Wilson, 1972;

Morgan, 1972a; O'Connor and Le Roex, 1992; Homrighausen et al., 2019; Geldmacher et al., 2005; Holm et al., 2008; Montelli et al., 2006; French and Romanowicz, 2015). The Sierra Leone Rise is also proposed to have been formed by a ridge-centered mantle plume in the late Cretaceous (Emelyanov et al., 1990). Accordingly, it was speculated that both the Sierra Leone Rise and the BSP were formed by the same Sierra Leone hotspot (Morgan, 1981; Schilling et al., 1994), currently assumed to be located east of the Mid-Atlantic ridge (MAR, Schilling et al., 1994).

During RV Maria S. Merian expedition MSM70 in 2018, high-resolution mapping and systematic rock sampling of the BSP and adjacent areas were conducted in order to constrain the origin of these seamounts and their magmatic sources (van der Zwan et al., 2018). In this study, we present petrological observations and a comprehensive geochemical data set (major and trace elements, and Sr-Nd-Pb-Hf isotope ratios) of volcanic rocks that were collected from 21 BSP seamounts and from the shoulder of a fracture zone northwest of the BSP (Cape Verde Ridge, see Figure 1b). With this dataset, we aim to evaluate the contrasting models for the origin of the BSP.

2. Geological background

The BSP is located in the Sierra Leone basin, which is intersected by a complex pattern of strike-slip transform faults. The Sierra Leone basin formed after the breakup of Gondwana and its evolution comprises three main phases, i.e., the pre-rift, rift, and post-rift (passive margin phase) (e.g., Nürnberg and Müller, 1991; Moulin et al., 2010), with the onset of seafloor spreading constrained to be in the early Cretaceous (at ~120 Ma, Jones et al., 1995; Nürnberg and Müller, 1991; Seton et al. 2012).

Two poorly investigated bathymetric anomalies, the Sierra Leone Rise and the adjacent BSP dominate the northern part of the Sierra Leone Basin. The Sierra Leone Rise is a ~600 km long and 400 km wide oceanic plateau that is mostly covered by Late Cretaceous and younger sediments (Lancelot et al., 1977). The Sierra Leone Rise and the conjugate Ceará Rise (now located on the South American plate; Figure 1a) are proposed to have formed as paired aseismic ridges by a ridge-centered mantle plume in the late Cretaceous (i.e., 80-90 Ma) (Emelyanov et al., 1990, Jones et al., 2015). Formation of these ridges ceased in the early Paleocene (~ 60 Ma) (Hekinian et al., 1978) and the plateaus subsequently drifted apart. The Sierra Leone Rise was drilled during Deep Sea Drilling Project (DSDP) Leg 3 (Site 13) and Leg 41 (Site 366, Lancelot et al., 1977) and Ocean Drilling Project (ODP) Leg 108 (Sites 665-668, Ruddiman et al., 1989),

but unfortunately no oceanic basement was recovered. Only a sediment core retrieved near Site 366 contained alkali-rich volcanic rock fragments that were, however, highly altered (Hekinian et al., 1978). Altered basaltic glasses recovered from the MAR at 1.7°N and the mantle-derived rocks from tectonically uplifted ridge fragments that form the nearby St. Peter and Paul rocks possess enriched geochemical signatures attributed to a postulated Sierra Leone plume (Schilling et al., 1994). The exact present location of this plume, however, was proposed to lie 100 km east of 1.7°N MAR anomaly (see Figure 1a, Schilling et al., 1994). Other hotspots in the vicinity of the BSP are the Cape Verde (~860 km to the north), Canary (~2300 km to the north), Ascension (~1750 km to the southwest) and St. Helena (~2800 km to the southeast) hotspots (see Figure 1a).

The BSP forms a >600 km long and ~170 km wide, NE-SW striking belt of irregular-shaped seamounts and elongated ridges stretching along the northwestern flank of the Sierra Leone Rise (Figure 1). To the north, the seamount belt is confined by the Guinea Fracture Zone, which is connected by a NW-SE striking fault (“Cutting Fault” in Figure 1) with the Vema Fracture Zone in the NW. Vertical gravity gradient data shows that the northern BSP edifices are located over several E-W oriented lineaments that terminate at the Cutting Fault/Guinea Fracture Zone (Sandwell et al., 2014). The seamount province consists of two

seamount groups: 1) the northern group between 7-9°N latitude, consisting primarily of NE-SW elongated volcanic structures partly overlying E-W oriented fracture zones, and 2) the southern group, consisting of E-W oriented seamounts, in an area where fracture zone traces are not obvious on satellite gravity maps. Near the BSP, the northern shoulder of the Cutting Fault forms a steep topographic high called Cape Verde Ridge (Figure 1b).

Detailed bathymetric mapping revealed that the edifices of the BSP range from 5 to 139 km in length/diameter and from 710 to 3930 m in height (van der Zwan et al., 2018). The shallowest seamounts (Annan and Arroyo seamounts) reach a minimum depth of about 210 m below sea level and are located on the northern and southern ends of the seamount belt. In contrast to the massive Sierra Leone Rise, most of the BSP (up to 62%) are flat-topped seamounts or guyots (Hess, 1946), indicating that they were most likely former ocean island volcanoes, which were eroded to wave base and then subsided to their present depths. Dredging shows that they are now capped by carbonate platforms, covered by manganese-iron or phosphorite crusts (e.g., Jones and Goddard, 1979; Jones et al., 2002; Skolotnev et al., 2017). The age of the underlying oceanic basement varies from ~60 Ma beneath the southwestern end and more than 100 Ma beneath the northeastern end of the BSP (see Figure 1b, Müller et al., 2016). Radiometric ages

are only available from a few sites thus far. In the north, volcanic samples from Carter Seamount yielded U-Pb zircon ages of 57-58 Ma (58 ± 1 and 57 ± 1.5 Ma) (Skolotnev et al., 2010) and ^{40}Ar - ^{39}Ar dating of phenocrysts from lamprophyre breccias from Prince Albert Seamount (also referred to Krause Seamount) gave ages ranging from 53.3-55.4 Ma (Jones et al., 1991, see Figure 1b). In addition, biotite phenocrysts from a basalt sample from Nadir Seamount gave a well-constrained ^{40}Ar - ^{39}Ar age of 58.6 ± 0.7 Ma (Bertrand et al., 1993, see Figure 1b). Although this seamount is offset ~350 km to the east of the BSP, Bertrand et al. (1993) interpreted it to be formed from the same magma source as the BSP, due to its similar age and major and trace element composition to the Prince Albert Seamount. Considerably younger ages of 36-43 Ma, determined by whole rock K-Ar dating of two trachybasalts from Prince Albert Seamount (Kharin et al., 1988, see Figure 1b), are believed to be underestimated due to the altered nature of the samples (Skolotnev et al., 2012), although they could also represent late-stage volcanism as is commonly found on seamounts. A whole rock K-Ar age of 37 Ma derived in the same study (Kharin et al., 1988) for a trachyte from Arroyo Seamount (also known as Nephrite Seamount, see Figure 1b) at the southern end of the BSP is also questionable. Nannofossils and foraminifers from a limestone sample obtained from the nearby Gilg Seamount (Figure 1b) provide a minimum stratigraphic age of 40-46 Ma (Skolotnev et al., 2017) for this volcanic structure. In

177 summary, even if we only consider the U/Pb zircon, ^{40}Ar - ^{39}Ar and nannofossil ages,
178 there could be a crude younging from NE to SW.

179
180 Geochemical data for volcanic samples were only reported from three northern
181 (Annan, Carter and Prince Albert / Krause; Kharin et al., 1988; Jones et al., 1991;
182 Peyve and Skolotnev, 2009; Skolotnev et al., 2012) and three southern (Gilg,
183 Cigogne and Arroyo; Kharin et al., 1988; Skolotnev et al., 2017) seamounts, but
184 systematic sampling of the BSP has not been carried out thus far. Previously
185 recovered lavas have compositions ranging from trachybasalts to trachyandesites to
186 trachytes (Kharin et al., 1988; Jones et al., 1991). The majority of the previously
187 recovered lava samples are highly altered (with loss on ignition (LOI) values up to
188 14.3%) (Peyve and Skolotnev, 2009; Skolotnev et al., 2012, 2017). Therefore, only
189 immobile elements and isotope data from leached samples should be considered.
190 The strong enrichment of highly incompatible elements over less incompatible
191 elements, coupled with the depletion of heavy rare earth elements (HREE), was
192 interpreted to reflect an ocean island basalt (OIB) composition formed by relatively
193 small degrees of partial melting at a high pressure with residual garnet (Peyve and
194 Skolotnev, 2009; Skolotnev et al., 2012, 2017). Samples from three different BSP
195 seamounts (Carter, Gilg and Cigogno) have widely varying isotopic compositions,
196 forming a weak trend from DM (Depleted Mantle) to HIMU (high μ = time-

integrated $^{238}\text{U}/^{204}\text{Pb}$) mantle end member compositions but with some samples deviating towards EM II (Enriched Mantle) composition (Skolotnev et al., 2012, 2017) (see section 4.3 for details).

3. Sampling and analytical methods

During RV Maria S. Merian expedition MSM70 (van der Zwan et al., 2018), igneous rocks were dredged from 25 sites evenly distributed along the entire BSP as well as from one site on the Cape Verde Ridge, the northern bounding fracture zone. The locations of the sampling sites are shown in Figure 1b and coordinates and further details are given in Table A1 (Appendix). Representative samples from all areas were selected for geochemical analysis based on the freshness of hand specimen and thin section inspection.

3.1. Major and trace element analyses

Altered outer surfaces of selected samples were removed with a rock saw, and the samples were subsequently crushed in a steel jaw crusher and dry sieved into 2mm, 1mm and 0.5mm fractions. Each size fraction was washed with deionized water in an ultrasonic bath 3 times for 15 minutes. The freshest fragments from the 1-2 mm fraction were carefully hand-picked under a binocular microscope, including both

phenocrysts and groundmass, in proportions to be representative for the bulk rocks to avoid a modification of its composition. Powders were made in an agate mortar and agate ball mill. Major elements were measured on fused glass beads by X-ray fluorescence spectroscopy (XRF) at the Institute of Mineralogy and Petrography at the University of Hamburg. Comparisons of international reference standards JB-2 and -3, JA-3 and JG-3 that were measured along with the lavas with the accepted values (Govindaraju 1994) yield accuracies better than 3% for SiO₂, TiO₂, Fe₂O₃, MgO, Na₂O and CaO, better than 5% for Al₂O₃ and K₂O, better than 10% for P₂O₅, and better than 15% for MnO (see Table A2).

Trace elements (Li, Sc, V, Cr, Co, Ni, Zn, Ga, Rb, Sr, Y, Zr, Nb, Ta, Cd, Cs, Ba, Hf, Pb, Th, U and all naturally-occurring REE) were determined from mixed acid (HF-aqua regia-HClO₄) pressure digests with an AGILENT 7500cs inductively coupled plasma mass spectrometer (ICP-MS) at the Institute of Geosciences, Kiel University. Details of the analytical procedure are given in Garbe-Schönberg (1993). The international reference standard BHVO-2, measured with the samples, gave trace element accuracies better than 3% for Li, Sc, V, Cr, Co, Ni, Ga, Rb, Sr, Y, Zr, Nb, Ba, U and all REE, better than 5% for Tm, better than 10% for Zn, Hf, Ta, Pb, and Th, and better than 12% for Cs (Jochum et al., 2016, see Table A3).

235

236 **3.2. Sr-Nd-Pb-Hf isotope geochemistry**

237 A total of 18 samples, from seamounts covering the entire seamount province and
238 the Cape Verde Ridge, were selected for Sr-Nd-Pb-Hf isotope analysis (Table 2).

239

240 Sr-Nd-Pb isotope measurements were conducted on rock chips. Approximately
241 100-250 mg sample chips were mildly leached in 2N HCl at 70 °C for one hour and
242 then triple rinsed in 18.2 MΩ water. Additional Sr isotope analyses were carried
243 out on 100 mg of whole rock powders with a stronger leach in 6N HCl at 150 °C
244 overnight followed by triple rinsing of the residue in 18.2 MΩ H₂O to remove
245 possible seawater alteration products. Both sample types were dissolved in a 5:1
246 mixture of concentrated HF and HNO₃ at 150 °C over 48 hours. Ion
247 chromatography analyses followed established standard procedures of Hoernle et
248 al. (2008). Sr, Nd and Pb isotopes were measured at GEOMAR with a Thermo
249 Fisher Scientific TRITON Plus thermal ionization mass spectrometer (TIMS)
250 operating in static mode.

251

252 Nd and Sr isotope ratios were normalized within the analytical run to $^{146}\text{Nd}/^{144}\text{Nd} =$
253 0.7219 and $^{86}\text{Sr}/^{88}\text{Sr} = 0.1194$, respectively. NBS987 and La Jolla standards were

measured 4-5 times in each sample turret and gave $^{87}\text{Sr}/^{86}\text{Sr} = 0.710268 \pm 0.000008$ (2SD, $n = 11$) and $^{143}\text{Nd}/^{144}\text{Nd} = 0.511845 \pm 0.000006$ (2SD, $n = 4$) respectively. Sample data are reported relative to $^{87}\text{Sr}/^{86}\text{Sr} = 0.710250$ and $^{143}\text{Nd}/^{144}\text{Nd} = 0.511850$. Of the powder samples undergoing the stronger leach, 13 of 18 samples produced lower $^{87}\text{Sr}/^{86}\text{Sr}$ ratios (0.00001-0.00359 lower) compared to the mildly-leached rock chips, while the 5 remaining samples gave higher $^{87}\text{Sr}/^{86}\text{Sr}$ ratios (0.00001-0.00033 higher) but with many being within error of each other. The lowest $^{87}\text{Sr}/^{86}\text{Sr}$ ratios obtained for a sample is presumed to be closest to its primary magmatic value and is thus reported in Table 2.

The Pb double spike (DS) technique of Hoernle et al. (2011b) was used to correct for instrumental mass bias. The long-term DS corrected NBS981 values are $^{206}\text{Pb}/^{204}\text{Pb} = 16.9407 \pm 0.0017$, $^{207}\text{Pb}/^{204}\text{Pb} = 15.4976 \pm 0.0018$, $^{208}\text{Pb}/^{204}\text{Pb} = 36.7201 \pm 0.0045$, $^{207}\text{Pb}/^{206}\text{Pb} = 0.914814 \pm 0.000039$, and $^{208}\text{Pb}/^{206}\text{Pb} = 2.167564 \pm 0.000082$ (2SD, $n = 120$).

Hf chemistry was conducted on 200-300 mg of unleached rock powder following the method of Blichert-Toft et al. (1997) and the measurements were performed on a Thermo Fisher Scientific NEPTUNE Plus MC-ICPMS at GEOMAR. Instrumental mass bias correction applied an exponential mass fractionation law

using the natural $^{179}\text{Hf}/^{177}\text{Hf}$ ratio of 0.7325. Drift corrected $^{176}\text{Hf}/^{177}\text{Hf}$ yielded =
0.282170 \pm 6 (n= 46) for our in-house Hf SPEX CertiPrepTM solution which
corresponds to $^{176}\text{Hf}/^{177}\text{Hf}$ = 0.282163 for JMC-475 (Blichert-Toft et al., 1997).

Total procedural blanks are < 20 pg for Pb, < 60 pg for Nd and Hf and < 100 pg for
Sr and thus negligible with respect to the amounts measured in the sample.

Sample (46DR-1) was replicated for Sr-Nd-Pb-Hf isotope ratios by digesting a
second set of mildly leached chips and strongly leached powders. While $^{87}\text{Sr}/^{86}\text{Sr}$,
 $^{143}\text{Nd}/^{144}\text{Nd}$, $^{206}\text{Pb}/^{204}\text{Pb}$, $^{207}\text{Pb}/^{204}\text{Pb}$, $^{208}\text{Pb}/^{204}\text{Pb}$ and $^{176}\text{Hf}/^{177}\text{Hf}$ ratios were all
reproduced within the external 2SE of each other, $^{87}\text{Sr}/^{86}\text{Sr}$ of the strongly leached
powders differ by 0.000018 and thus slightly outside the 0.000016 2SD bar of
NBS987, which most likely reflects variability in removal of seawater altered
domains. Reference material BCR-2 was processed for Sr-Nd-Pb and Hf under
similar conditions as the samples. Results are listed in Table 2 and compare well
with those of Fourny et al (2016) and Todd et al (2015).

4. Results

4.1 Petrography

293 The volcanic samples dredged from the BSP comprise dense lavas and
294 volcanoclastic tuff breccias containing volcanic pebbles (van der Zwan et al.,
295 2018). Both rock types were recovered throughout the entire BSP and the dense
296 lavas and volcanic clasts embedded in the breccias dredged from the same
297 seamounts show no distinct differences. Volcanic samples from the northern BSP
298 are generally dark grey in color and have a high percentage of vesicles (20-50
299 vol.%) that are partially filled with secondary minerals such as zeolite and opal.
300 These rocks are porphyritic (5-30 vol.% phenocrysts) with the phenocryst
301 assemblage primarily consisting of pyroxene ($\leq 30\%$), plagioclase ($\leq 10\%$) and
302 amphibole ($\leq 4\%$), with sporadic apatite. The groundmass has an intersertal texture
303 with abundant microlites of plagioclase and pyroxene and considerable Fe-Ti
304 oxides. In contrast, samples from the central and southern BSP are generally grey
305 and brown-grey and contain a slightly lower percentage of vesicles (10-40 vol.%),
306 which are also partially filled by secondary minerals such as zeolite, calcite and
307 opal. These rocks are also porphyritic (2-25 vol.% phenocrysts) and contain, in
308 addition to plagioclase ($\leq 15\%$) and clinopyroxene ($\leq 10\%$), also olivine ($\leq 5\%$),
309 abundant amphibole ($\leq 20\%$) and biotite ($\leq 2\%$) phenocrysts. The groundmass also
310 has an intersertal texture but with higher contents of plagioclase, reduced amount
311 of pyroxenes and scarce microlites of amphibole, Fe-Ti oxide and secondary
312 iddingsite (an alteration product of olivine). Noteworthy is that the volcanic

samples from the BSP XVII Seamount (69DR) have a unique appearance with a pale grey matrix color and apparent flow textures.

Lavas dredged from the Cape Verde Ridge (the Cutting Fault shoulder) are dark grey, non-vesicular and dense. They generally are completely crystalline and have a diabasic texture containing a mineral assemblage of plagioclase ($\leq 50\%$), clinopyroxene (20-45%) and chlorite (5-20%). Only one sample (5DR-5) is porphyritic with a phenocryst assemblage consisting of plagioclase (~6%), pyroxene (~1%) and (secondary) chlorite (~3%), the groundmass has an intersertal texture with abundant microlites of plagioclase and a considerable amount of Fe-Ti oxides.

4.2 Major and trace elements

Major and trace element data are shown in Table 1.

The MgO contents of samples both from the BSP and Cape Verde Ridge range from 0.49-11.2 wt%, whereas their Ni and Cr concentrations are below 300 ppm and 600 ppm, respectively. Therefore, most magmas underwent crystal fractionation and the present composition of the lavas doesn't reflect the composition of the primitive melts (Figure 2). For the BSP lavas, MgO correlates

negatively with SiO_2 , Al_2O_3 , Na_2O and K_2O and incompatible elements, and positively with compatible trace elements such as Ni (incorporated in olivine) and Sc (clinopyroxene). The kink in the CaO trend at $\text{MgO} = 8\%$ and the decreasing trend of $\text{CaO}/\text{Al}_2\text{O}_3$ indicate the onset and fractionation of clinopyroxene (in addition to olivine). The kinks in the trends of FeO_T and TiO_2 at $\text{MgO} = 6 \text{ wt}\%$ indicate fractionation of Ti-magnetite. In contrast to the northern BSP samples, the southern BSP samples are relatively evolved ($\text{MgO} < 6 \text{ wt}\%$). Since amphibole is observed in thin sections (see section 4.1), the decrease of CaO with simultaneous increase in alkali content is also consistent with calcic amphibole fractionation. All BSP samples, particularly those from southern BSP with increased amphibole contents (see section 4.1), show a decrease in TiO_2 at $\text{MgO} < 6 \text{ wt}\%$, which reflects fractionation of Fe-Ti oxides and possibly fractionation of the Ti-bearing amphibole such as kaersutite. Samples from the Cape Verde Ridge, however, do not lie on the same crystal fractionation trends as the BSP samples but possess higher SiO_2 and Na_2O , but lower FeO_T , TiO_2 , CaO and P_2O_5 at a given MgO content, reflecting a more tholeiitic composition of these samples compared to the alkalic (silica-undersaturated) compositions of the BSP samples.

When dealing with old, submarine samples, caution is required regarding the potential effect of seawater alteration on the concentration of mobile elements such

as Na and K, which are generally used for rock classification. Therefore, classification schemes of Pearce (2008) utilizing only relatively fluid-immobile elements are used for this study (Figure 3). All samples plot within the mantle array with the lavas from the BSP falling within the OIB field (Figure 3a) consistent with alkali OIB-like compositions (Figure 3b). Note that several samples from the southern and central BSP (e.g., 36DR-1, 38DR-5, 39DR-1, 69DR-2) are relatively evolved ($\text{MgO} < 6\text{wt.}\%$). Therefore TiO_2 content has been diminished by differentiation and the TiO_2/Yb ratios will be lower than those of the parental melts. As a result, we do not include data for samples with $\text{MgO} < 6\text{wt.}\%$ in Figure 3b.

On multi-element diagrams, the samples from the BSP show similar patterns with enrichment of highly- to less-incompatible elements (e.g. $[\text{La}/\text{Sm}]_{\text{N}} = 2.1\text{-}18.3$ where N denotes normalization to primitive mantle), as is characteristic for OIB lavas (Figure 4). The distinct enrichment in Nb and Ta and a marked depletion in Pb resemble the pattern of HIMU-type OIBs (Willbold and Stracke, 2006) (Figure 4). In addition, BSP samples show fractionated heavy rare earth element patterns (e.g. $[\text{Ce}/\text{Yb}]_{\text{N}} = 7.34 - 32.7$, see Figure 4).

The rocks from the Cape Verde Ridge differ markedly from the BSP lavas in their trace element compositions (Figures 3 and 4). In contrast to the BSP seamounts,

the two samples from the Cape Verde Ridge have tholeiitic composition with 5DR-5 plotting in the normal mid-ocean ridge basalt (N-MORB) region and 5DR-8 in the tholeiitic ocean-island-basalt (OIB) range (see Figure 3). Accordingly, Cape Verde Ridge lava 5DR-5 possesses low ratios of highly- over less-incompatible elements, resembling N-MORB (Figure 4b). Sample 5DR-8 shows more enrichment in highly- relative to less-incompatible elements but is still less enriched than the alkalic BSP lavas (Figure 4b). In addition, 5DR-8 shows a moderate depletion in heavy rare earth elements ($[Ce/Yb]_N=4.95$, see Figure 4b).

4.3. Sr-Nd-Pb-Hf isotopes

For the first time, we present a comprehensive Sr-Nd-Pb-Hf isotope data set, corrected for radiogenic ingrowth, from both the BSP and the adjacent Cape Verde Ridge in Table 2 and Figure 5.

Seawater alteration can disturb the isotope systems of submarine samples, particularly if they are tens of millions of years old and involve elements of low ionic potential (i.e., fluid-mobile) such as the Rb-Sr and U-Pb systems. Uranium gain from seawater or Pb gain/loss as a result of hydrothermal alteration could lead to disturbed parent/daughter relationships, resulting in potential over-correction (due to U addition or Pb loss) or undercorrection (due to U loss or Pb gain) when

correcting the isotope ratios for radiogenic ingrowth. As this issue cannot be solved by strong acid-leaching that could further fractionate the U and Pb concentrations, the extent of post-eruptive U gain and Pb gain/loss in the old submarine lavas was evaluated by their internal trace element correlations compared to fluid immobile elements (e.g., Th/U and Nd/Pb ratios, see Figure A1 (Appendix)). No significant U gain/loss or Pb gain/loss is indicated by this method for the majority of the samples selected for isotope measurements, with the exception of 5DR-8 (Pb loss), 49R-2 (Pb gain), 23DR-1, 55DR-4 and 57DR-1-4 (both U loss and Pb gain). Consequently, these samples are marked with open symbols in Figure 5. The majority of isotope samples possess μ values ($^{238}\text{U}/^{204}\text{Pb}$) between 8 and 41, which fall within the range proposed for mantle sources including HIMU (12-61; Stracke et al., 2003). We therefore conclude that secondary disturbance of the U-Pb system in most samples was not significant.

Based on the available radiometric age determinations, an average age of 50 Ma was chosen for calculating the initial isotope ratios of the BSP and Cape Verde Ridge samples (Jones et al. (1991), Skolotnev et al. (2010) and Skolotnev et al. (2017)).

412 Consistent with their enriched trace element compositions, the BSP lavas have
 413 reasonably enriched initial isotopic ratios (assuming that they were formed at 50
 414 Ma): $^{87}\text{Sr}/^{86}\text{Sr}_{\text{in}} = 0.70322\text{-}0.70390$, $^{143}\text{Nd}/^{144}\text{Nd}_{\text{in}} = 0.51263\text{-}0.51282$, $^{206}\text{Pb}/^{204}\text{Pb}_{\text{in}}$
 415 $= 19.22\text{-}20.37$, $^{207}\text{Pb}/^{204}\text{Pb}_{\text{in}} = 15.60\text{-}15.71$, $^{208}\text{Pb}/^{204}\text{Pb}_{\text{in}} = 39.18\text{-}40.22$ and
 416 $^{176}\text{Hf}/^{177}\text{Hf}_{\text{in}} = 0.28289\text{-}0.28302$. The Pb isotope data show a wide variation,
 417 trending from a depleted mantle end member (e.g., VEMA Fracture Zone) towards
 418 a HIMU-like mantle end member composition, with the samples with most
 419 radiogenic $^{206}\text{Pb}/^{204}\text{Pb}$ ratios, however, being slightly offset from the Atlantic and
 420 Pacific HIMU end-members of St. Helena and Austral Islands, respectively
 421 (slightly higher $^{208}\text{Pb}/^{204}\text{Pb}_{\text{in}}$ and lower $^{143}\text{Nd}/^{144}\text{Nd}_{\text{in}}$ for a given $^{206}\text{Pb}/^{204}\text{Pb}_{\text{in}}$, Figure
 422 5). Considering the age uncertainties for the BSP lavas, the significance of this
 423 offset is unclear. The lavas that form the depleted end of the BSP trend partially
 424 overlap the fields for the 1.7 °N MAR anomaly and St. Peter and Paul rocks.
 425
 426 The new isotope data partly overlap the composition of the few previously
 427 published BSP samples by Skolotnev et al. (2012, 2017) that were derived from
 428 three BSP seamounts from which we also sampled for this study. Our initial
 429 isotope data, however, display a wider range in $^{206}\text{Pb}/^{204}\text{Pb}$ but a much narrower
 430 spread in $^{143}\text{Nd}/^{144}\text{Nd}$ and $^{207}\text{Pb}/^{204}\text{Pb}$ showing no involvement of an EM II
 431 component (see section 5.1).

432

433 Neither the different (geographic) segments of the BSP (i.e., northern, central and
434 southern segments) nor the different flanks (eastern and western sides) show
435 distinct isotopic differences. One sample (49DR-2) from the southern section of
436 the BSP has an anomalously high $^{207}\text{Pb}/^{204}\text{Pb}_{\text{in}}$ (15.71) at relatively low
437 $^{206}\text{Pb}/^{204}\text{Pb}_{\text{in}}$ (19.22) ratio, but this rock experienced post-magmatic disturbance of
438 its U-Pb system (see above) and is therefore shown with an open sample symbol in
439 Figure 5. We note that some of the literature data also show the same deviation
440 towards higher $^{207}\text{Pb}/^{204}\text{Pb}$ and ascribe this shift to the effect of seawater alteration,
441 but it is still difficult to explain the excess $^{207}\text{Pb}/^{204}\text{Pb}$ unless additional old Pb
442 (with high $^{207}\text{Pb}/^{204}\text{Pb}$) has been added to the sample.

443

444 The two analyzed samples from the Cape Verde Ridge display a surprisingly large
445 range in isotopic composition. The N-MORB-like sample 5DR-5 plots close to the
446 field of local MORB and the Vema Fracture Zone lavas (projected to 50 Ma ago),
447 but has slightly lower $^{143}\text{Nd}/^{144}\text{Nd}_{\text{in}}$ and $^{176}\text{Hf}/^{177}\text{Hf}_{\text{in}}$ ratios for a given $^{206}\text{Pb}/^{204}\text{Pb}_{\text{in}}$.
448 Tholeiitic OIB lava 5DR-8 (with moderately enriched incompatible-element
449 compositions) has the most radiogenic (St. Helena HIMU-type) isotopic
450 composition of all lavas analyzed in this study (with a range in $^{206}\text{Pb}/^{204}\text{Pb}_{\text{in}}$ of
451 19.22-20.44, Figure 5). Both samples have elevated initial Sr isotopic composition

(>0.704) compared to the other samples analyzed in this study, which no doubt reflects uptake of seawater Sr in these samples.

5. Discussion

5.1 Source characteristics of the BSP and the Cape Verde Ridge

The dredged BSP lavas show typical alkali OIB compositions (Figure 3), consistent with the seamounts having formed in an intraplate oceanic setting as previously assumed by Skolotnev et al. (2017). The distinct enrichment of highly incompatible elements over less incompatible elements and presumably of volatiles (as indicated by the amphibole and biotite phenocrysts) in the lavas suggests that the BSP seamounts were formed by small degrees of partial melting (Figure 4) from enriched sources. Small degrees of partial melting are consistent with melting beneath a relatively mature oceanic plate (~30-40 Ma at the time of BSP formation, see Figure 1), with a thickness of 60-70 km (when applying the half space cooling model of Stein and Stein (1992)). The strong depletion of heavy rare earth elements (HREE) in the BSP samples ($(\text{Tb/Yb})_N = 2.21 - 2.80$) and the high TiO_2/Yb ($\text{TiO}_2/\text{Yb} = 1.17\text{-}2.20$, for samples with $\text{MgO} > 6$ wt.%) are likely to indicate the presence of garnet in their mantle source (Figures 3 and 4). Comparing our samples to the model of Yokoyama et al. (2007), using La/Yb to estimate

degrees of partial melting and Gd/Yb for residual source mineralogy (specifically, the phase containing aluminium), also suggests low degrees of partial melting (less than 4%, except for one outlier from the central BSP area) and residual garnet (Figure 6). The model of Yokoyama et al. (2007) assumes pure peridotitic melting. Montanini and Tribuzio (2015) and Niu and Batiza (1997) showed that pyroxenite present in the form of veins in peridotite can have enriched isotopic compositions. Our whole rock data set does not give any conclusive evidence on the mineralogy of the source. Nevertheless, even if a pyroxenite component was present, the depleted HREE signature still requires the presence of garnet and thus melt must have formed at depth of at least 40-50 km (the stability field of garnet-pyroxenite; Hirschmann and Stolper, 1996; Sobolev et al., 2007; Zindler and Hart, 1986). HREE depletion, on the other hand, has also been associated with amphibole in the magma source (Rooney et al., 2017; Pilet et al., 2008) and could potentially explain the strong K-depletion and variable Ba/Nb in the samples. However, the same signatures could be obtained by fractional crystallization of amphibole, as is present in many of our samples as phenocrysts (see section 4.1). In addition, a strong depletion of K (Figure 4) is characteristic of HIMU magmas. K/La versus Yb/La shows no correlation (not shown), therefore indicating that the depletion of the HREE is not caused by an influence of amphibole but reflects small degrees of melting in the presence of garnet (as also suggested by the amphibole-lherzolite

melting model of Marzoli et al., 2000). High H₂O contents are also consistent with small-degrees of melting since H₂O acts as an incompatible element in deep magmatic systems (Michael, 1995; Gibson and Richards, 2018). We speculate that the formation of the nearby SLR could have caused metasomatism of the surrounding asthenosphere and lithosphere (Rooney, 2020; Gibson and Richards, 2018). If, for example, ascending plume material encounters volatile-rich parts of the asthenosphere/lithosphere, melting will be stimulated and volatiles will preferentially enter the initial melts. It's indicative that hydrous phases (such as amphibole) are found in lavas from BSP seamounts (formed in immediate vicinity of the SLR) but not in lavas from the Cape Verde Ridge (located furthest away from the SLR).

The isotopic composition of the BSP lavas can be interpreted to reflect a mixture between a depleted mantle component, comparable to the local MORB source (or VEMA fracture zone), and an enriched HIMU-like isotopic composition, similar, but not identical, to St. Helena and Cook-Austral end member HIMU (see calculated mixing lines of potential endmembers in Figure 5). The HIMU mantle source has been traditionally related to recycled oceanic crust (Hofmann and White, 1982). Seismic low velocity conduits (interpreted to reflect upwelling mantle plumes) have been imaged extending to the base of the lower mantle beneath the St.

511 Helena and Cook-Austral Islands (e.g., Montelli et al., 2006; French and
512 Romanowitz, 2015), suggesting a deep mantle origin for the HIMU component.
513 Alternative models for HIMU genesis involve recycling of ancient (≥ 2.5 Ga)
514 metasomatized subcontinental lithospheric mantle through the lower mantle
515 (Homrighausen et al., 2018; Scott et al., 2014; Weiss et al., 2016).

516

517 The BSP lavas fall on an extension of the St. Peter and Paul Rocks and the 1.7 N
518 MAR anomaly compositional field, which may imply that they share the same
519 enriched end member. Unfortunately, the lack of isotope data from the Sierra
520 Leone Rise leaves the question open if the same enriched end member also
521 contributed to the formation of this large plateau.

522

523 Our data set does not support a significant contribution of an EM-like mantle end
524 member as proposed by Skolotnev et al. (2012, 2017). We note that those four
525 previously published samples from the southern BSP (grey triangles in Figure 5)
526 that show low $^{143}\text{Nd}/^{144}\text{Nd}$ and high $^{207}\text{Pb}/^{204}\text{Pb}$, trending in the direction of EM II,
527 also possess very high $^{87}\text{Sr}/^{86}\text{Sr}$ ratios (Figure 5a). The combination of radiogenic
528 $^{207}\text{Pb}/^{204}\text{Pb}$ and $^{87}\text{Sr}/^{86}\text{Sr}$ but relatively unradiogenic $^{143}\text{Nd}/^{144}\text{Nd}$, together with their
529 depletion of Ce and enrichment of Y (see Figure 4 of Skolotnev et al., 2017)),

530 points to assimilation of pelagic sediments or to postmagmatic incorporation of
531 sediment and or manganese/phosphorite.

532

533 Although recovered in the same dredge haul, the two Cape Verde Ridge samples
534 attest to distinct origins of their melts. Depleted sample 5DR-5 has typical N-
535 MORB compositions in major and trace elements and isotopes. The flat HREE
536 patterns on the multi-element diagrams, indicate that garnet was not a residual
537 phase when this melt was formed (Figure 4). This no doubt reflects a combination
538 of higher degrees of melting and a shallower depth of origin. It is therefore likely
539 that this melt formed in the shallow upper mantle beneath the MAR and that the
540 rock thus represents the local oceanic crust (consistent with being sampled at a
541 fracture zone). Therefore, the 5DR-5 isotopic compositions could serve as the
542 potential end member for the local depleted upper mantle.

543

544 In contrast, sample 5DR-8 has an enriched geochemical composition which is
545 isotopically similar to the most enriched BSP lavas, but it differs from them in
546 several respects: 1) It has a tholeiitic rather than alkalic composition (Figure 3b); 2)
547 It formed through higher degrees of partial melting (Figures 4 and 6), and 3) It has
548 a less-fractionated HREE pattern (low $(\text{Tb/Yb})_{\text{N}} = 1.61$), reflecting less residual

garnet in its source after melting (see Figures 4 and 6). Therefore, this enriched Cape Verde Ridge lava cannot have formed from the same (MORB) magma source as the depleted Cape Verde Ridge rock 5DR-5. In comparison to the BSP lavas, this tholeiitic lava is likely to have formed at comparatively higher degrees of partial melting and at a shallower depth than the alkalic BSP lavas. Its similar isotopic composition to some of the BSP samples, however, implies derivation from the same source (see section 5.3).

5.2 The origin of the Bathymetrists Seamount Province

Due to the sparseness of previously available samples, the creation of the BSP is still a topic of debate. In principle, the seamounts could have formed by the following processes: 1) Shallow decompression melting of enriched material due to extension along local tectonic fissures or fracture zones (e.g., the leaky fracture zone model) (Jones, 1987; Jones et al., 1991; Skolotnev et al., 2010; 2012); 2) Melting due to small scale sub-lithosphere convection (e.g. King and Anderson, 1998; King and Ritsema 2000; Milelli et al 2012; Ballmer et al., 2009; Reusch et al., 2010), as a result of the breakup of Gondwana (separation of the South America from the Northwest Africa) or differences in oceanic lithosphere thickness; 3) Melting of plume/hotspot material from a deep source (e.g. Kharin,

1988). In the following sections, we will evaluate each of these models in the light of the newly obtained data.

1) Formation by upper mantle decompression melting along fracture zones

The location of the BSP overlying a series of fracture zones, and the shape and E-W orientation of the southern BSP seamounts that stretch e.g. along latitudes of 7°N and 9°N could potentially be explained by decompression melting due to extension along local tectonic fissures (e.g., the leaky fracture zone model as suggested by e.g. Jones (1987), Jones et al. (1991) and Skolotnev et al. (2010, 2017)). This model would explain the distinctly younger ages of these BSP edifices (Jones et al., 1991; Skolotnev et al., 2010) compared to the underlying oceanic basement as the transform faults were active after the formation of the oceanic crust. Small amounts of geochemically enriched metasomatized subcontinental mantle or delaminated lower continental crust retained in the upper mantle after Gondwana breakup would be more fusible during partial melting (Jones, 1991; Peyve and Skolotnev, 2009; Skolotnev et al., 2010) and could explain the observed trace element enrichment, the presence of amphibole in some of the lavas (consistent with a volatile-rich source), and potentially also their HIMU-like isotopic signature if the lithospheric mantle had an Early Proterozoic or Archean

age (Weiss et al., 2016; Homrighausen et al. 2018). However, the evidence for residual garnet during formation of the BSP lavas argues for deeper melting (≥ 80 km if the source was peridotitic) and is thus not consistent with this hypothesis. Although large faults can potentially cut through the entire lithosphere, its base would still lie at 60-70 km depths (Section 5.1), which is above the upper limit of the garnet peridotite stability zone. In pyroxenitic material, however, garnet would be stable to more shallow depth (see above). Most importantly, it is highly questionable if decompression melting due to extension at a fracture zone will create a sufficient volume of melt. The majority of the BSP seamounts are guyots that once formed ocean islands. The seamounts that formed at 7° N latitude (that would best reflect melting along fracture zones) comprise a combined volume of approximately $8,532 \text{ km}^3$ (calculated by treating the circular Maria S. Merian Seamounts as two truncated cones, and the coalescent Gilg and Webb Seamount ridge as truncated rectangular pyramid). Since the heights of the former subaerial summits are unknown, this number represents only a minimum value. Considering a ratio of 1:5 for extrusive to intrusive volumes of ocean island volcanism (Crisp, 1984), results in a total igneous volume of $51,194 \text{ km}^3$. Assuming an average degree of 2% partial melting (see Figure 6), $2.56 \times 10^6 \text{ km}^3$ of mantle material would be needed to produce the igneous volume of the seamounts along 7° N. The melting zone can be roughly imagined as a ~ 200 km long rectangle (reaching from

the western edge of Maria S. Merian Seamounts to the eastern edge of Webb Seamount). Assuming melting started around 80 km depth (to accommodate for the garnet signature) and continued almost to the surface (which is unrealistic), this melting zone would need to be 160 km wide, which is more than five times the widths of the seamounts/structures along 7 °N (~30 km). Since incipient melts will not be funneled towards the fracture zone (in contrast to the melting regime beneath mid-ocean ridges), the effective collection of melts from such a large region appears unrealistic. Narrowing the melting zone to about 30 km would require that melting starts already at 427 km depth, which is well below the lithosphere base, making decompression melt by faults unlikely, and is only possible at elevated mantle temperatures and continuous (active) upwelling (i.e. presence of a mantle plume). Even if we assume that this area of the upper mantle is composed of hydrous peridotite (maybe caused by volatile metasomatism during the formation of the nearby Sierra Leone Rise plateau), which would begin melting significantly deeper than dry peridotite at a given temperature (Katz et al., 2003), the solidus at regular mantle temperatures would lie at ~5 GPa or 160 km depth (Ito and Mahoney, 2005).

2) Formation by small-scale upper mantle convection

Volcanism caused by small-scale, edge-driven convection has been proposed and applied to volcanism along the margin of lithospheres with different thicknesses to explain volcanic provinces without clear age progressions (e.g. Cameroon Volcanic Line; King and Anderson, 1998; King and Ritsema 2000; Milelli et al 2012; Reusch et al., 2010). In the area of the BSP, multiple variations in lithosphere thickness are present. After the breakup of the central Atlantic and with the onset of seafloor spreading, the thick continental lithosphere of the old NW African craton (i.e., the old part of the African continental lithosphere, see Figure 1) was juxtaposed with thin, young and relatively hot oceanic lithosphere. The differences in lithosphere thickness and temperature variations could have caused local mantle upwelling resulting in decompression melting. The HIMU-like signature could originate from delamination of the metasomatized subcontinental lithospheric mantle of the Africa craton that is eroded by the convection currents (e.g. Geldmacher et al., 2005; Kipf et al., 2014). A potential problem with this model is the oblique orientation of the BSP compared to both the edge of African continent and the West-African Craton that is difficult to explain with this model, it is also unclear if this mechanism is capable of producing large enough volumes of melt by low degrees of melting to create the BSP (see above).

645 A better fit for causing small-scale mantle convection would be the directly
646 neighboring Sierra Leone Rise plateau with which the BSP share the same
647 orientation. Schade (2018) proposed this model based on the model from Ballmer
648 et al. (2007), who proposed that small-scale, sub-lithospheric convection always
649 initiates if the cold thermal boundary layer beneath the oceanic lithosphere
650 surpasses a threshold thickness of 60-100 km (Ballmer et al., 2007). Due to the
651 assumed formation of the Sierra Leone Rise by a ridge-centered plume and
652 possible additional underplated magmatism, the Sierra Leone Rise exhibits an
653 anomalously thick igneous crust of up to 17 km and Moho depths of up to 20 km
654 (Jones et al., 2015). Therefore, a thickened oceanic lithospheric mantle beneath the
655 Sierra Leone Rise may be possible. Under this thickened lithosphere, edge-driven
656 convection transformed into rolls aligned with plate motion with the upwelling
657 areas reaching a diameter up to 200-300 km (Richter and Parsons, 1975, Ballmer et
658 al., 2007). The local tectonic weakness could contribute to further melting, leading
659 to the BSP formation. This model might explain why the BSP stretches subparallel
660 to the Sierra Leone Rise. As the upwelling (and eventually melting) starts beneath
661 thickened lithosphere, it could also explain the presence of garnet in the source. It
662 is questionable, however, if upwelling material could reach the northeastern and
663 the southwestern extent of the BSP (> 400 km outside of the Sierra Leone Rise
664 area) and explain the high volume of the BSP seamounts (see above). In addition,

the Sierra Leone Rise is situated on ~20 Ma younger oceanic crust than the oldest crust under the northern BSP and thus has a ~40 km thinner underlying lithosphere (Stein and Stein, 1992), making this model highly unlikely.

3) Formation by a mantle plume

The formation of the BSP by melting of upwelling material from a hotspot (mantle plume) beneath a thick lithospheric lid would be consistent with 1) the low degree of partial melting at depths in excess of 70-80 km and alkaline character of the samples, 2) the end member HIMU-like isotopic composition, similar to St. Helena where a mantle plume has been imaged to the base of the lower mantle, 3) supply of a sufficiently large amount of fertile mantle to produce the large volume of low-degree melts that form the BSP, and 4) the crude NE to SW age progression (according to the limited available age data) and overall orientation of the BSP in the direction of plate motion, mimicing the strike of other Atlantic hotspot tracks on the African Plate.

Could the BSP have formed from a Sierra Leone mantle plume that previously produced the paired Sierra Leone and C  ar    Rise and the isotopic signature of St. Peter and Paul Rocks and the 1.7  N MAR anomaly? The cessation of the aseismic

ridge formation and the beginning of the separation of the Sierra Leone and C  ar   Rise (~60 Ma, Hekinian et al., 1978) coincides with the ages obtained for the northern BSP Prince Albert / Krause and Carter seamounts (53-58 Ma) (Jones et al., 1991; Skolotnev et al., 2010). The compositional fields of the 1.7  N MAR anomaly and St. Peter and Paul rocks fall on the same trend on binary isotope diagrams as the BSP lavas. The slightly less radiogenic isotopic signatures of the 1.7  N MAR anomaly lavas (Schilling et al., 1994) are consistent with dilution of the enriched plume signature by interaction with the nearby spreading center (e.g., Long et al., 2019). The relation of such a postulated Sierra Leone plume to the BSP, however, is ambiguous: The only geochemical data available to date are major element compositions of clinopyroxene phenocrysts obtained from the Sierra Leone Rise and C  ar   Rise lavas reported in Fodor and Hekinian (1981). Their composition overlaps with the composition spanned by clinopyroxene phenocrysts from the Carter Seamount on the BSP (Schade, 2018), but no whole rock major and trace element and no isotope data from whole rocks or clinopyroxene phenocrysts are available from the Sierra Leone Rise and its conjugate C  ar   Rise.

A major problem for this model is that the BSP is located to the northwest of the Sierra Leone Rise, which does not fit plate tectonic reconstructions (Sleep, 2002). An explanation could be that with progressively increasing distance from the

westward-migrating MAR, the Sierra Leone plume no longer fed the spreading axis but instead switched to a plume-fracture zone interaction, in which the transform faults to the north of the Sierra Leone Rise provided the pathways to channel the ascending melts. Nevertheless, most BSP seamounts are oriented NE-SW, which is not consistent with plume-fracture zone interaction being the main cause for the origin of the BSP. In addition, modern plate tectonic reconstructions do not place the BSP anywhere near the assumed current location of the postulated Sierra Leone hotspot (100 km east of 1.7 °N MAR anomaly, see Figure 1, Schilling et al., 1994). Instead, assuming that the BSP hotspot track originates at the ~58 Ma Carter Seamount, our calculation shows that the current position of an assumed stationary hotspot for the BSP should be located at 5.28 °N, 25.3 °W (see Figure 1), which is offset by ~700 km from the Sierra Leone hotspot location assumed by Schilling et al (1994) and is marked by a prominent cluster of BSP seamounts (slightly outside our sampling area).

Seismic tomographic models such as SEMUCB-WM1 show a slow seismic velocity anomaly beneath the extrapolated location of the present hotspot (Figure 7). It is therefore possible that the BSP was created by a hotspot distinct from the postulated Sierra Leone mantle plume, which could be in its waning stage, considering that the width of the BSP and the number of individual seamounts

pinch out towards the SW. We also see that the low-velocity anomaly does not clearly extend beneath ~500 km, although there is an area of slower velocities directly beneath the present hotspot location, between two areas of fast velocities. Due to the resolution of global tomography and narrow conduit with diameter of 100-200 km diameter cannot be clearly resolved. Alternatively, this could indicate pulse-like upwellings from the lower mantle beneath 1000 km or that a plume-like upwelling is dying out, explaining why the size and density of seamounts at the SW end of the BSP decreases. It is noteworthy to point out that the BSP lavas provide another example of extreme HIMU end member composition supporting the view of Homrighausen et al. (2018) that such composition is more widespread than previously thought. In the case of the BSP hotspot proposed here, the enriched endmember plume composition seems to be best represented by Cape Verde Ridge dredge sample 5DR-8 (see Figure 5). Its composition overlaps within error of St. Helena lavas except in Sr isotopic composition, which is likely to reflect seawater alteration, i.e. exchange/addition of some very radiogenic seawater Sr to the sample. More age dating, however, is necessary to confirm the crude age progression seen in the very limited published age data.

5.3 The origin of the lavas sampled at the Cape Verde Ridge

743 The different geochemical character of the samples recovered from the same
744 dredge haul at the Cape Verde Ridge fracture zone shoulder indicates that two
745 fundamentally different volcanic units were sampled. The N-MORB like lava
746 (sample 5DR-5) most likely represents the local oceanic crust generated by normal
747 mid-ocean ridge melting, unrelated to the BSP. The enriched tholeiitic OIB lava
748 (sample 5DR-8), however, was obtained from a volcanic unit genetically related to
749 and possibly best represents the BSP hotspot magma source. In contrast to the BSP
750 alkalic lavas, this tholeiitic sample's composition is consistent with higher degrees
751 and shallower melting. Since this sample was recovered from a fracture zone, local
752 extension could have allowed greater decompression melting to shallower depth of
753 enriched BSP source material than beneath the BSP, thus explaining the tholeiitic
754 rather than alkalic composition of this sample (Figure 3b). This would require that
755 BSP plume materials spread out in the upper mantle at least 100 km beyond the the
756 location of the Annan Seamount (the most northwestern seamount, Figure 1b),
757 possibly facilitated/controlled by the steep step at the base of the lithosphere
758 beneath the Cutting Fault. It is unclear, however, that the fault was still active
759 approximately 50 Ma later after the lithosphere creation. On the other hand, it has
760 been shown that Shona plume material flowed ≥ 600 km along the base of the
761 Agulhas fracture zone and then produced enough melt to form the Agulhas Ridge
762 in the fracture zone (Hoernle et al., 2016).

763

764 **6. Conclusions**

765 Our new and comprehensive geochemical data set obtained from detailed sampling
766 of the BSP confirms that this broad belt of seamounts was formed in an intraplate
767 setting. Due to the large volume of low degree melts needed to form the extensive
768 BSP and the deep origin of the melts, we can exclude shallow decompression
769 melting related to extension as the sole cause of melt production. The distinct
770 HIMU-like isotopic composition of the magmas argues against derivation from the
771 nearest central/south Atlantic hotspots (Cape Verde and Ascension). Small-scale
772 edge driven convection along the lithospheric base of the adjacent Sierra Leone
773 Rise or the postulated Sierra Leone plume cannot explain the currently available
774 geochemical and age data and the plate tectonic reconstructions. To the contrary,
775 the presence of the isotopically enriched HIMU-like end-member type composition
776 in some of the lavas, a crude age progression in the direction of plate motion, the
777 low-velocity anomaly extending to depths of ≥ 500 km below SW end of the
778 province, the large volume of low-degree melts forming the BSP and our plate
779 tectonic reconstruction provide evidence that this seamount province was
780 generated by a distinct hotspot that is currently located at 5.28 °N, 25.3 °W. This
781 location is marked by a prominent seamount cluster and is still underlain by a

slow seismic velocity conduit. Locally, magma ascent might be controlled by extensional faulting related to the different subsidence rate of the thicker SLR (compared to the surrounding regular oceanic lithosphere) or along fracture zones. More age data are needed to confirm the age progression of the BSP as predicted by this model.

7. Acknowledgements

We thank Captain Ralf Schmidt and his crew for their support during the MSM70 cruise, the Leitstelle Deutsche Forschungsschiffe for the organization of the cruise and the MSM70 scientific party for their help in obtaining the samples. In addition, we are very grateful to Silke Hauff, Karin Junge, Marcus Gutjahr (all GEOMAR) and Ulrike Westernströer (Kiel University) for their help with the sample analysis. X.L. was funded by the China Scholarship Council (CSC). Analytical work was funded by the DFG (MSM70 initial postcruise funding) and GEOMAR. We thank Catherine Chauvel for editorial handling of this manuscript and Dennis Geist, Tyrone Rooney and one anonymous reviewer for providing constructive reviews.

References

- Ballmer, M. D., Van Hunen, J., Ito, G., Tackley, P. J., and Bianco, T. A., 2007. Non-hotspot volcano chains originating from small-scale sublithospheric convection. *Geophysical Research Letters* 34, <https://doi.org/10.1029/2007GL031636>.
- Ballmer, M. V., Van Hunen, J., Ito, G., Bianco, T. A., and Tackley, P. J., 2009. Intraplate volcanism with complex age-distance patterns: A case for small-scale sublithospheric convection. *Geochemistry, Geophysics, Geosystems* 10, <https://doi.org/10.1029/2009GC002386>.
- Barker, A. K., Holm, P. M., Peate, D. W., and Baker, J. A., 2010. A 5 million year record of compositional variations in mantle sources to magmatism on Santiago, southern Cape Verde archipelago. *Contributions to Mineralogy and Petrology* 160, 133-154.
- Begg G C, Griffin W L, Natapov L M, et al., 2009. The lithospheric architecture of Africa: Seismic tomography, mantle petrology, and tectonic evolution. *Geosphere* 5, 23-50.
- Bercovici, D., Ricard, Y., and Richards, M. A., 2000. The relation between mantle dynamics and plate tectonics: A primer. *Geophysical Monograph-American Geophysical Union* 121, 5-46.
- Bertrand, H., Féraud, G., and Mascle, J., 1993. Alkaline volcano of Paleocene age on the Southern Guinean Margin: Mapping, petrology, ^{40}Ar - ^{39}Ar laser probe dating, and implications for the evolution of the Eastern Equatorial Atlantic. *Marine geology* 114, 251-262.
- Blichert-Toft, J., Chauvel, C., and Albarède, F., 1997. Separation of Hf and Lu for high-precision isotope analysis of rock samples by magnetic sector-multiple collector ICP-MS. *Contributions to Mineralogy and Petrology* 127, 248-260.
- Burke K, Wilson J T., 1972. Is the African plate stationary?. *Nature* 239, 387-390.
- Burke, K., Steinberger, B., Torsvik, T. H., and Smethurst, M. A., 2008. Plume generation zones at the margins of large low shear velocity provinces on the core–mantle boundary. *Earth and Planetary Science Letters* 265, 49-60.
- Chaffey, D., Cliff, R., and Wilson, B., 1989. Characterization of the St Helena magma source. *Geological Society, London, Special Publications* 42, 257-276.

825 Chauvel, C., Hofmann, A. W., and Vidal, P., 1992. HIMU-EM: the French Polynesian connection. *Earth and*
 826 *Planetary Science Letters* 110, 99-119.

827 Crisp, J. A., 1984. Rates of magma emplacement and volcanic output. *Journal of Volcanology and Geothermal*
 828 *Research* 20, 177-211.

829 Dosso, L., Bougault, H., and Joron, J.-L., 1993. Geochemical morphology of the North Mid-Atlantic Ridge,
 830 10-24 °N: Trace element-isotope complementarity. *Earth and Planetary Science Letters* 120, 443-462.

831 Doucelance, R., Hammouda, T., Moreira, M., and Martins, J. C., 2010. Geochemical constraints on depth of
 832 origin of oceanic carbonatites: the Cape Verde case. *Geochimica et Cosmochimica Acta* 74, 7261-7282.

833 Duncan, R. A., and McDougall, I., 1976. Linear volcanism in French polynesia. *Journal of volcanology and*
 834 *geothermal research* 1, 197-227.

835 Emelyanov, E., Elnikov, I., Trimonis, E., and Kharin, G., 1990. Geology of the Sierra Leone Rise. *Geologische*
 836 *Rundschau* 79, 823-848.

837 Fodor, R. V., and Hekinian, R., 1981. Petrology of basaltic rocks from the ceara and the sierra-leone aseismic
 838 rises in the equatorial atlantic-ocean. *Oceanologica Acta* 4, 223-228.

839 Foulger, G. R., 2005. Mantle plumes: Why the current skepticism. *Chinese Science Bulletin* 50, 1555-1560.

840 Fourny, A., Weis, D., and Scoates, J. S., 2016. Comprehensive Pb-Sr-Nd-Hf isotopic, trace element, and
 841 mineralogical characterization of mafic to ultramafic rock reference materials. *Geochemistry,*
 842 *Geophysics, Geosystems* 17, 739-773.

843 French, S. W. and Romanowicz, B. A., 2014. Whole-mantle radially anisotropic shear velocity structure
 844 from spectral-element waveform tomography. *Geophysical Journal International* 199, 1303-1327.

845 French, S. W. and Romanowicz, B., 2015. Broad plumes rooted at the base of the Earth's mantle beneath major
 846 hotspots. *Nature* 525, 95-99.

847 Gale, A., Dalton, C. A., Langmuir, C. H., Su, Y., and Schilling, J. G., 2013. The mean composition of ocean
 848 ridge basalts. *Geochemistry, Geophysics, Geosystems* 14, 489-518,
 849 <https://doi.org/10.1029/2012GC004334>.

850 Garbe-Schönberg, C. D., 1993. Simultaneous determination of thirty-seven trace elements in twenty-eight
 851 international rock standards by ICP-MS. *Geostandards and Geoanalytical Research* 17, 81-97.

852 Geldmacher J, Hoernle K, Bogaard P, et al., 2005. New $^{40}\text{Ar}/^{39}\text{Ar}$ age and geochemical data from seamounts in
853 the Canary and Madeira volcanic provinces: support for the mantle plume hypothesis. *Earth and Planetary*
854 *Science Letters* 237, 85-101.

855 Geldmacher J, Hoernle K, Kluegel A, et al., 2008. Geochemistry of a new enriched mantle type locality in the
856 northern hemisphere: Implications for the origin of the EM-I source. *Earth and Planetary Science Letters*
857 265, 167-182.

858 Govindaraju, K., 1994. Compilation of working values and sample description for 383 geostandards.
859 *Geostandards newsletter* 18, 1-158.

860 Hanyu, T., Tatsumi, Y., Senda, R., Miyazaki, T., Chang, Q., Hirahara, Y., and Nakai, S. I., 2011. Geochemical
861 characteristics and origin of the HIMU reservoir: A possible mantle plume source in the lower
862 mantle. *Geochemistry, Geophysics, Geosystems* 12, <https://doi.org/10.1029/2010GC003252>.

863 Hanyu, T., Dosso, L., Ishizuka, O., Tani, K., Hanan, B. B., Adam, C., and Tatsumi, Y., 2013. Geochemical
864 diversity in submarine HIMU basalts from Austral Islands, French Polynesia. *Contributions to*
865 *Mineralogy and Petrology* 166, 1285-1304.

866 Hauri, E. H., Shimizu, N., Dieu, J. J., and Hart, S. R., 1993. Evidence for hotspot-related carbonatite
867 metasomatism in the oceanic upper mantle. *Nature* 365, 221-227.

868 Hekinian R., 1978. Volcanics from the Sierra Leone Rise. *Nature* 257, 536-538

869 Hess, H. H., 1946. Drowned ancient islands of the Pacific Basin. *American Journal of Science* 244, 772-791.

870 Hieronymus, C. F., and Bercovici, D., 2000. Non-hotspot formation of volcanic chains: Control of tectonic and
871 flexural stresses on magma transport. *Earth and Planetary Science Letters* 181, 539-554.

872 Hirschmann M. M., and Stolper E. M., 1996. A possible role for garnet pyroxenite in the origin of the “garnet
873 signature” in MORB. *Contributions to Mineralogy and Petrology* 124: 185-208.

874 Hoernle, K., Abt, D. L., Fischer, K. M., Nichols, H., Hauff, F., Abers, G. A., Van Den Bogaard, P., Heydolph,
875 K., Alvarado, G., and Protti, M., 2008. Arc-parallel flow in the mantle wedge beneath Costa Rica and
876 Nicaragua. *Nature* 451, 1094-1097.

877 Hoernle, K., Hauff, F., Werner, R., van den Bogaard, P., Gibbons, A. D., Conrad, S., and Müller, R. D., 2011a.
878 Origin of Indian Ocean Seamount Province by shallow recycling of continental lithosphere. *Nature*
879 *Geoscience* 4, 883-887.

880 Hoernle, K., Hauff, F., Kokfelt, T. F., Haase, K., Garbe-Schönberg, D., and Werner, R., 2011b. On-and off-
881 axis chemical heterogeneities along the South Atlantic Mid-Ocean-Ridge (5-11 °S): shallow or deep
882 recycling of ocean crust and/or intraplate volcanism?: *Earth and Planetary Science Letters* 306, 86-97.

883 Hoernle, K., Schwindrofska, A., Werner, R., van den Bogaard, P., Hauff, F., Uenzelmann-Neben, G., and
884 Garbe-Schönberg, D., 2016. Tectonic dissection and displacement of parts of Shona hotspot volcano 3500
885 km along the Agulhas-Falkland Fracture Zone. *Geology* 44, 263-266.

886 Hofmann, A. W., and Hart, S. R., 1978. An assessment of local and regional isotopic equilibrium in the
887 mantle. *Earth and Planetary Science Letters* 38, 44-62.

888 Hofmann, A. W., and White, W. M., 1982. Mantle plumes from ancient oceanic crust. *Earth and Planetary*
889 *Science Letters* 57, 421-436.

890 Holm, P. M., Wilson, J. R., Christensen, B. P., Hansen, L., Hansen, S. L., Hein, K. M., Mortensen, A. K.,
891 Pedersen, R., Plesner, S., and Runge, M. K., 2005. Sampling the Cape Verde mantle plume: evolution of
892 melt compositions on Santo Antão, Cape Verde Islands. *Journal of Petrology* 47, 145-189.

893 Holm P M, Grandvuinet T, Friis J, et al., 2008. An ^{40}Ar - ^{39}Ar study of the Cape Verde hot spot: Temporal
894 evolution in a semistationary plate environment. *Journal of Geophysical Research: Solid Earth* 113,
895 <https://doi.org/10.1029/2007JB005339>.

896 Homrighausen, S., Hoernle, K., Hauff, F., Geldmacher, J., Wartho, J. A., van den Bogaard, P., and Garbe-
897 Schönberg, D., 2018. Global distribution of the HIMU end member: Formation through Archean plume-
898 lid tectonics. *Earth-science reviews* 182, 85-101.

899 Homrighausen, S., Hoernle, K., Hauff, F., Wartho, J. A., van den Bogaard, P., and Garbe-Schönberg, D., 2019.
900 New age and geochemical data from the Walvis Ridge: The temporal and spatial diversity of South
901 Atlantic intraplate volcanism and its possible origin. *Geochimica et Cosmochimica Acta* 245, 16-34.

902 Ito, G., and Mahoney, J. J., 2005. Flow and melting of a heterogeneous mantle: 1. Method and importance to
 903 the geochemistry of ocean island and mid-ocean ridge basalts. *Earth and Planetary Science Letters* 230,
 904 29-46.

905 Jochum, K. P., Weis, U., Schwager, B., Stoll, B., Wilson, S. A., Haug, G. H., and Enzweiler, J., 2016.
 906 Reference values following ISO guidelines for frequently requested rock reference
 907 materials. *Geostandards and Geoanalytical Research* 40, 333-350.

908 Jones E J W., 1987. Fracture zones in the equatorial Atlantic and the breakup of western Pangea. *Geology* 15:
 909 533-536.

910 Jones, E. J. W., and Goddard, D. A., 1979. Deep-sea phosphorite of Tertiary age from Annan Seamount,
 911 eastern equatorial Atlantic. *Deep Sea Research Part A. Oceanographic Research Papers* 26, 1363-1379.

912 Jones, E., Goddard, D., Mitchell, J., and Banner, F., 1991. Lamprophyric volcanism of Cenozoic age on the
 913 Sierra Leone Rise: implications for regional tectonics and the stratigraphic time scale. *Marine Geology* 99,
 914 19-28.

915 Jones, E. J. W., Cande, S. C., and Spathopoulos, F., 1995. Evolution of a major oceanographic pathway: the
 916 equatorial Atlantic. *Geological Society, London, Special Publications* 90, 199-213

917 Jones, E. J. W., BouDagher-Fadel, M. K., and Thirlwall, M. F., 2002. An investigation of seamount
 918 phosphorites in the Eastern Equatorial Atlantic. *Marine Geology* 183, 143-162.

919 Jones E J W, McMechan G A, Zeng X., 2015. Seismic evidence for crustal underplating beneath a large
 920 igneous province: The Sierra Leone Rise, equatorial Atlantic. *Marine Geology* 365: 52-60.

921 Katz, R. F., Spiegelman, M., and Langmuir, C. H., 2003. A new parameterization of hydrous mantle melting.
 922 *Geochemistry, Geophysics, Geosystems* 4, <https://doi.org/10.1029/2002GC000433>.

923 Kharin, G., 1988. The magmatic rocks of the Sierra Leone Rise (the Equatorial Atlantic) (in Russian).
 924 *Okeanologija* 28, 82-88.

925 King, S. D., and Anderson, D. L., 1998. Edge-driven convection. *Earth and Planetary Science Letters* 160,
 926 289-296.

927 King SD, Ritsema J, 2000. African hot spot volcanism: small-scale convection in the upper mantle beneath
 928 cratons. *Science* 290, 1137-1140

929 Kipf, A., Hauff, F., Werner, R., Gohl, K., van den Bogaard, P., Hoernle, K., and Klügel, A., 2014. Seamounts
 930 off the West Antarctic margin: A case for non-hotspot driven intraplate volcanism. *Gondwana*
 931 *Research* 25, 1660-1679.

932 Koppers, A. A., Staudigel, H., Pringle, M. S., and Wijbrans, J. R., 2003. Short-lived and discontinuous
 933 intraplate volcanism in the South Pacific: Hot spots or extensional volcanism?. *Geochemistry, Geophysics,*
 934 *Geosystems* 4, <https://doi.org/10.1029/2003GC000533>.

935 Lancelot Y, Seibold E, Cepek P, et al., 1977. Site 366: Sierra Leone Rise, *Proceedings of the Ocean Drilling*
 936 *Program, Part A: Initial Reports* 41: 21-161.

937 Long, X., Geldmacher, J., Hoernle, K., Hauff, F., Wartho, J. A., Garbe-Schönberg, D., and Grevenmeyer, I.,
 938 2019. Age and origin of Researcher Ridge and an explanation for the 14 °N anomaly on the Mid-Atlantic
 939 Ridge by plume-ridge interaction. *Lithos* 326, 540-555.

940 Long, X., Geldmacher, J., Hoernle, K., Hauff, F., Wartho, J. A., and Garbe-Schönberg, D., Origin of isolated
 941 seamounts in the Canary Basin (East Atlantic): The role of plume material in the origin of seamounts not
 942 associated with hotspot tracks (in review). submitted to *Terra Nova*.

943 Martins, S., Mata, J., Munh á J., Mendes, M. H., Maerschalk, C., Caldeira, R., and Mattielli, N., 2010.
 944 Chemical and mineralogical evidence of the occurrence of mantle metasomatism by carbonate-rich melts
 945 in an oceanic environment (Santiago Island, Cape Verde). *Mineralogy and Petrology* 99, 43-65.

946 Marzoli, A., Piccirillo, E. M., Renne, P. R., Bellieni, G., Iacumin, M., Nyobe, J. B., and Tongwa, A. T., 2000.
 947 The Cameroon Volcanic Line revisited: petrogenesis of continental basaltic magmas from lithospheric
 948 and asthenospheric mantle sources. *Journal of Petrology* 41, 87-109.

949 Maury, R. C., El Azzouzi, M., Bellon, H., Liotard, J. M., Guille, G., Barszczus, H. G., and Brousse, R., 1994.
 950 Géologie et pétrologie de l'île de Tubuai (Australes, Polynésie française). *Compte-Rendu de l'Académie*
 951 *des Sciences* 318, 1341-1347.

952 McDougall, I., 1971. Volcanic island chains and sea floor spreading. *Nature Physical Science* 231, 141-144.

953 Michael, P., 1995. Regionally distinctive sources of depleted MORB: Evidence from trace elements and H₂O.
 954 *Earth and Planetary Science Letters* 131, 301-320.

955 Milelli L, Fourel L, Jaupart C, 2012. A lithospheric instability origin for the Cameroon Volcanic Line. *Earth*

Planet Science Letters 335, 80-87.

Montanini, A. and Tribuzio, R., 2015. Evolution of recycled crust within the mantle: constraints from the garnet pyroxenites of the External Ligurian ophiolites (northern Apennines, Italy). *Geology* 43, 911-914.

Montelli, R., Nolet, G., Dahlen, F. A., and Masters, G., 2006. A catalogue of deep mantle plumes: New results from finite-frequency tomography. *Geochemistry, Geophysics, Geosystems* 7, <https://doi.org/10.1029/2006GC001248>.

Morgan, W. J., 1971. Convection plumes in the lower mantle. *Nature* 230, 42-43.

Morgan, W. J., 1972a. Deep mantle convection plumes and plate motions. *AAPG bulletin* 56, 203-213.

Morgan, W. J., 1972b. Plate motions and deep mantle convection. *Geol. Soc. Am. Man.* 132, 7-22.

Morgan, W. J., 1981. Hotspot tracks and the opening of the Atlantic and Indian Oceans. *The oceanic lithosphere* 7, 443-487.

Mourão, C., Mata, J., Doucelance, R., Madeira, J., Millet, M.-A., and Moreira, M., 2012. Geochemical temporal evolution of Brava Island magmatism: constraints on the variability of Cape Verde mantle sources and on carbonatite-silicate magma link. *Chemical Geology* 334, 44-61.

Müller R D, Seton M, Zahirovic S, et al., 2016. Ocean basin evolution and global-scale plate reorganization events since Pangea breakup. *Annual Review of Earth and Planetary Sciences* 44, 107-138.

Nakamura, Y., and Tatsumoto, M., 1988. Pb, Nd, and Sr isotopic evidence for a multicomponent source for rocks of Cook-Austral Islands and heterogeneities of mantle plumes. *Geochimica et Cosmochimica Acta* 52, 2909-2924.

Natland, J. H., and Winterer, E. L., 2005. Fissure control on volcanic action in the Pacific. *Special papers-Geological Society of America* 388, 687.

Nebel, O., Arculus, R. J., van Westrenen, W., Woodhead, J. D., Jenner, F. E., Nebel-Jacobsen, Y. J., and Eggins, S. M., 2013. Coupled Hf-Nd-Pb isotope co-variations of HIMU oceanic island basalts from Mangaia, Cook-Austral islands, suggest an Archean source component in the mantle transition zone. *Geochimica et cosmochimica acta* 112, 87-101.

Niu, Y. and Batiza, R., 1997. Trace element evidence from seamounts for recycled oceanic crust in the Eastern Pacific mantle. *Earth and Planetary Science Letters* 148, 471-483.

983 Niu Y, Regelous M, Wendt I J, et al. Geochemistry of near-EPR seamounts: importance of source vs. process
984 and the origin of enriched mantle component[J]. *Earth and Planetary Science Letters*, 2002, 199(3-4):
985 327-345.

986 Nürnberg, D., and Müller, R. D., 1991. The tectonic evolution of the South Atlantic from Late Jurassic to
987 present. *Tectonophysics* 191, 27-53.

988 O'Connor J M, le Roex A P., 1992. South Atlantic hot spot-plume systems: 1. Distribution of volcanism in
989 time and space. *Earth and Planetary Science Letters* 113, 343-364.

990 Paulick H, Münker C, Schuth S., 2010. The influence of small-scale mantle heterogeneities on Mid-Ocean
991 Ridge volcanism: evidence from the southern Mid-Atlantic Ridge (7° 30' S to 11° 30' S) and Ascension
992 Island. *Earth and Planetary Science Letters* 296, 299-310.

993 Pearce, J. A., 2008. Geochemical fingerprinting of oceanic basalts with applications to ophiolite classification
994 and the search for Archean oceanic crust. *Lithos* 100, 14-48.

995 Peyve, A., and Skolotnev, S., 2009. Alkali volcanism of the Bathymetrists Seamounts chain (Central Atlantic).
996 *Doklady Earth Sciences* 425, 243-248.

997 Pfänder, J. A., Münker, C., Stracke, A., and Mezger, K., 2007. Nb/Ta and Zr/Hf in ocean island basalts-
998 implications for crust-mantle differentiation and the fate of Niobium. *Earth and Planetary Science*
999 *Letters* 254, 158-172.

1000 Pilet, S., Baker, M. B., and Stolper, E. M., 2008. Metasomatized lithosphere and the origin of alkaline lavas.
1001 *Science* 320, 916-919.

1002 Reisberg, L., Zindler, A., Marcantonio, F., White, W., Wyman, D., and Weaver, B., 1993. Os isotope
1003 systematics in ocean island basalts. *Earth and Planetary Science Letters* 120, 149-167.

1004 Reusch A, Nyblade A, Wiens D, Shore P, Ateba B, Tabod C, Nnange J, 2010. Upper mantle structure beneath
1005 Cameroon from body wave tomography and the origin of the Cameroon Volcanic Line. *Geochem*
1006 *Geophys Geosyst* 11, <https://doi.org/10.1029/2010GC003200>.

1007 Richter, F. M., and Parsons, B., 1975. On the interaction of two scales of convection in the mantle. *Journal of*
1008 *Geophysical Research* 80, 2529-2541.

1009 Roden M K, Hart S R, Frey F A, et al., 1984. Sr, Nd and Pb isotopic and REE geochemistry of St. Paul's Rocks:
 1010 the metamorphic and metasomatic development of an alkali basalt mantle source. Contributions to
 1011 Mineralogy and Petrology 85, 376-390.

1012 Rooney, T. O., Nelson, W. R., Ayalew, D., Hanan, B., Yirgu, G., and Kappelman, J., 2017. Melting the
 1013 lithosphere: Metasomes as a source for mantle-derived magmas. Earth and Planetary Science Letters 461,
 1014 105-118.

1015 Rooney, T.O., 2020. The Cenozoic Magmatism of East Africa: Part V - Magma Sources and Processes in the
 1016 East African Rift. Lithos. Doi: 10.1016/j.lithos.2020.105381

1017 Ruddiman, W. F., Sarnthein, M., Backman, J., Baldauf, J. G., Curry, W., Dupont, L. M., and Stein, R., 1989.
 1018 Late Miocene to Pleistocene evolution of climate in Africa and the low-latitude Atlantic: Overview of Leg
 1019 108. In Proceedings of the Ocean Drilling Program Scientific Results 108, 463-484.

1020 Sager, W. W., Huang, Y., Tominaga, M., Greene, J. A., Nakanishi, M., and Zhang, J., 2019. Oceanic plateau
 1021 formation by seafloor spreading implied by Tamu Massif magnetic anomalies. Nature Geoscience 12,
 1022 661-666.

1023 Salters, V. J. M., White W. M., 1998. Hf isotope constraints on mantle evolution. Chemical Geology 145,
 1024 447-460.

1025 Salters V. J. M., Mallicks., Hart S. R., Langmuir C. H., Stracke A., 2011. Domains of depleted mantle: New
 1026 evidence from hafnium and neodymium isotopes. Geochemistry, Geophysics, Geosystems 12.
 1027 <https://doi.org/10.1029/2011GC003617>

1028 Sandwell, D. T., Müller, R. D., Smith, W. H., Garcia, E., and Francis, R., 2014. New global marine gravity
 1029 model from CryoSat-2 and Jason-1 reveals buried tectonic structure. Science 346, 65-67.

1030 Schade M., 2018. The structural and geomorphological connection of the Bathymetrists Seamounts and the
 1031 Sierra Leone Rise, Central Eastern Atlantic (available by contacting mschade@geomar.de)

1032 Schiano, P., Burton, K. W., Dupre, B., Birck, J. L., Guille, G., and Allegre, C. J., 2001. Correlated Os-Pb-Nd-
 1033 Sr isotopes in the Austral-Cook chain basalts: the nature of mantle components in plume sources. Earth
 1034 and Planetary Science Letters 186, 527-537.

1035 Schilling, J. G., Hanan, B. B., McCully, B., Kingsley, R., and Fontignie, D., 1994. Influence of the Sierra
 1036 Leone mantle plume on the equatorial Mid-Atlantic Ridge: A Nd-Sr-Pb isotopic study. *Journal of*
 1037 *Geophysical Research: Solid Earth* 99, 12005-12028.

1038 Scott, J. M., Waight, T. E., Van der Meer, Q. H. A., Palin, J. M., Cooper, A. F., and Münker, C., 2014.
 1039 Metasomatized ancient lithospheric mantle beneath the young Zealandia microcontinent and its role in
 1040 HIMU-like intraplate magmatism. *Geochemistry, Geophysics, Geosystems* 15, 3477-3501,
 1041 <https://doi.org/10.1002/2014GC005300>.

1042 Seton, M., Müller, R., Zahirovic, S., Gaina, C., Torsvik, T., Shephard, G., Talsma, A., Gurnis, M., Turner, M.,
 1043 and Maus, S., 2012. Global continental and ocean basin reconstructions since 200 Ma. *Earth-Science*
 1044 *Reviews* 113, 212-270.

1045 Skolotnev, S., Bel'Tenev, V., Lepekhina, E., and Ipat'eva, I., 2010. Younger and older zircons from rocks of
 1046 the oceanic lithosphere in the Central Atlantic and their geotectonic implications. *Geotectonics* 44, 462-
 1047 492.

1048 Skolotnev, S., Petrova, V., and Peyve, A., 2012. Origin of submarine volcanism at the eastern margin of the
 1049 central atlantic: Investigation of the alkaline volcanic rocks of the carter seamount (Grimaldi Seamounts).
 1050 *Petrology* 20, 59-85.

1051 Skolotnev, S., Peyve, A., Bylinskaya, M., and Golovina, L., 2017. New data on the composition and age of
 1052 rocks from the Bathymetrists Seamounts (Eastern margin of the equatorial Atlantic). in *Proceedings*
 1053 *Doklady Earth Sciences* 472, 20-25.

1054 Sleep, N. H., 1984. Tapping of magmas from ubiquitous mantle heterogeneities: an alternative to mantle
 1055 plumes?. *Journal of Geophysical Research: Solid Earth* 89, 10029-10041.

1056 Sleep, N. H., 2002. Ridge-crossing mantle plumes and gaps in tracks. *Geochemistry, Geophysics, Geosystems*
 1057 3, <https://doi.org/10.1029/2001GC000290>.

1058 Sobolev, A. V., Hofmann, A. W., Kuzmin, D. V., Yaxley, G. M., Arndt, N. T., Chung, S.-L., Danyushevsky, L.
 1059 V., Elliott, T., Frey, F. A., and Garcia, M. O., 2007, The amount of recycled crust in sources of mantle-
 1060 derived melts. *Science* 316, 412-417.

1061 Stein, C. A., and Stein, S., 1992. A model for the global variation in oceanic depth and heat flow with
 1062 lithospheric age. *Nature* 359, 123-129.

1063 Stracke, A., Bizimis, M., and Salters, V. J., 2003. Recycling oceanic crust: Quantitative
 1064 constraints. *Geochemistry, Geophysics, Geosystems* 4, <https://doi.org/10.1029/2001GC000223>.

1065 Stracke, A., Hofmann, A. W., and Hart, S. R., 2005. FOZO, HIMU, and the rest of the mantle
 1066 zoo. *Geochemistry, Geophysics, Geosystems* 6, <https://doi.org/10.1029/2004GC000824>.

1067 Sun, S.-S., and McDonough, W.-s., 1989. Chemical and isotopic systematics of oceanic basalts: implications
 1068 for mantle composition and processes. *Geological Society, London, Special Publications* 42, 313-345.

1069 Todd, E., Stracke, A., and Scherer, E. E., 2015. Effects of simple acid leaching of crushed and powdered
 1070 geological materials on high-precision Pb isotope analyses. *Geochemistry, Geophysics, Geosystems*
 1071 16, 2276-2302.

1072 Torsvik T H, Smethurst M A, Burke K, et al., 2006. Large igneous provinces generated from the margins of
 1073 the large low-velocity provinces in the deep mantle. *Geophysical Journal International* 167: 1447-1460.

1074 van der Zwan, F. M., 2018. BATHYCHEM The effect of intraplate volcanism on the geochemical evolution of
 1075 oceanic lithosphere: Detailed mapping and sampling of the Bathymetrists Seamounts and adjacent
 1076 fracture zones, December 26, 2017-February 01, 2018 Mindelo (Cape Verde)-Las Palmas de Gran
 1077 Canaria, Canary Islands (Spain), <http://oceanrep.geomar.de/id/eprint/45754>.

1078 Vidal, P., Chauvel, C., and Brousse, R., 1984. Large mantle heterogeneity beneath French
 1079 Polynesia. *Nature* 307, 536-538.

1080 Waters C L, Sims K W W, Perfit M R, et al. Perspective on the genesis of E-MORB from chemical and
 1081 isotopic heterogeneity at 9–10 N East Pacific Rise[J]. *Journal of Petrology*, 2011, 52(3): 565-602.

1082 Weiss Y, Class C, Goldstein S L, et al. , 2016. Key new pieces of the HIMU puzzle from olivines and diamond
 1083 inclusions. *Nature* 537, 666-670.

1084 White, W. M., 2010. Oceanic island basalts and mantle plumes: the geochemical perspective. *Annual Review*
 1085 *of Earth and Planetary Sciences* 38, 133-160.

1086 Whittaker J M, Afonso J C, Masterton S, et al., 2015. Long-term interaction between mid-ocean ridges and
 1087 mantle plumes. *Nature Geoscience* 8, 479-483.

1088 Willbold, M., and Stracke, A., 2006. Trace element composition of mantle end-members: Implications for
 1089 recycling of oceanic and upper and lower continental crust. *Geochemistry, Geophysics, Geosystems* 7,
 1090 <https://doi.org/10.1029/2005GC001005>.

1091 Wilson, J. T., 1963. A possible origin of the Hawaiian Islands: *Canadian Journal of Physics* 41, 863-870.

1092 Woodhead, J. D., 1996. Extreme HIMU in an oceanic setting: The geochemistry of Mangaia Island (Polynesia),
 1093 and temporal evolution of the Cook-Austral hotspot. *Journal of Volcanology and Geothermal Research* 72,
 1094 1-19.

1095 Workman, R. K., and Hart, S. R., 2005. Major and trace element composition of the depleted MORB mantle
 1096 (DMM). *Earth and Planetary Science Letters* 231, 53-72.

1097 Yokoyama T, Aka F T, Kusakabe M, et al., 2017. Plume-lithosphere interaction beneath Mt. Cameroon
 1098 volcano, West Africa: constraints from ^{238}U - ^{230}Th - ^{226}Ra and Sr-Nd-Pb isotope systematics. *Geochimica et*
 1099 *Cosmochimica Acta* 71, 1835-1854.

1100 Zindler, A., and Hart, S., 1986. Chemical geodynamics. *Annual review of earth and planetary sciences* 14,
 1101 493-571.

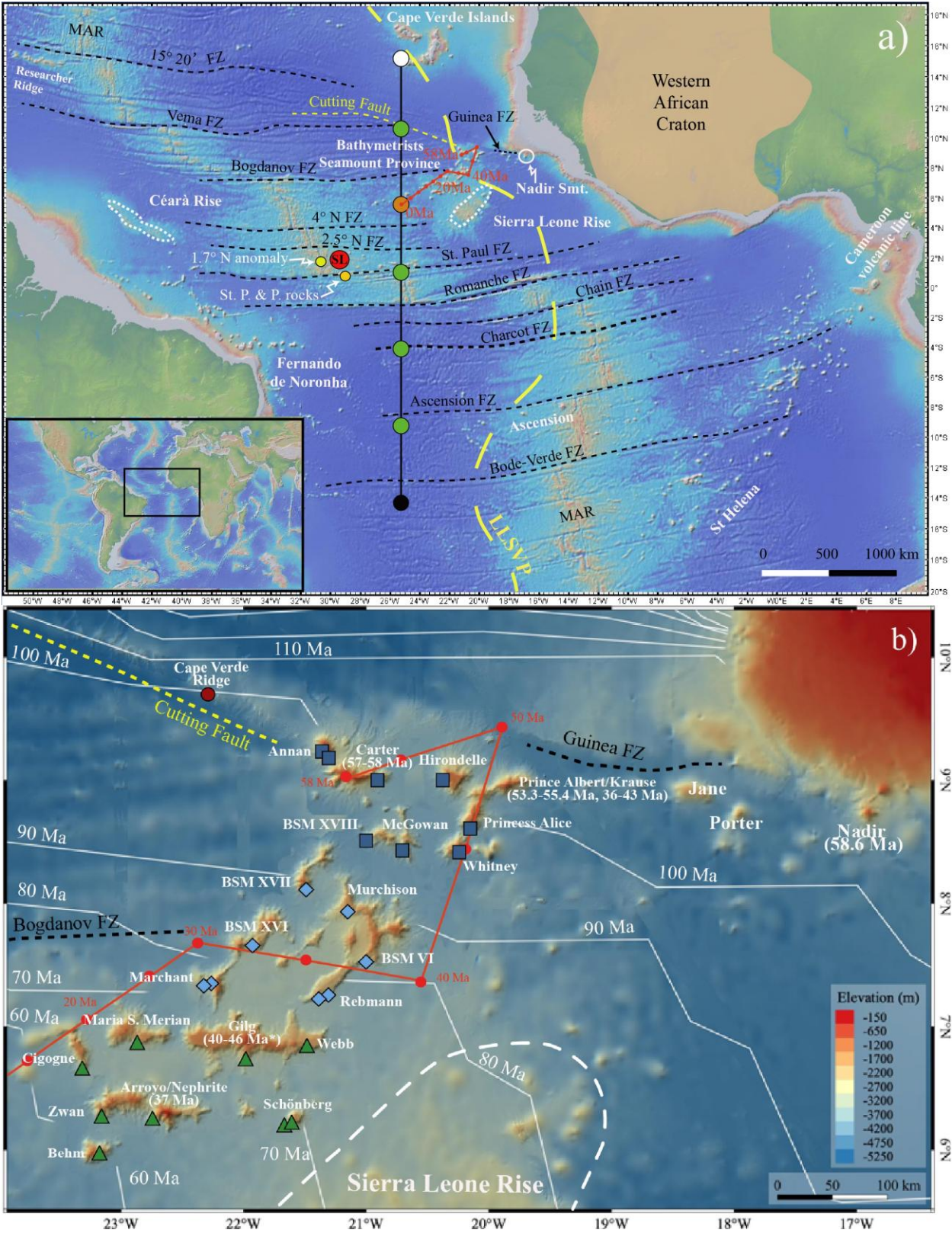


Figure 1. a) Overview map of the Central Atlantic Ocean showing the location of the Bathymetrists

Seamount Province (BSP), the Sierra Leone Rise and other topographic features including the 1.7°N MAR anomaly on the MAR and St. Peter and Paul Rocks (St. P.&P. rocks) postulated to reflect interaction with the Sierra Leone plume (Bertrand et al., 1993; Roden et al., 1984), which is proposed to be ~100 km to the east of the 1.7°N MAR anomaly (marked with red circle labeled SL) (Schilling et al., 1994). The red line shows the modeled path of the African plate (with 5 Ma increments) above a potential fixed hotspot (starting at Carter Seamount at ~58 Ma, Skolotnev et al., 2010) by using rotation parameters of Seton et al. (2012) and the GPlates software from Müller et al. (2016). The current location of the hotspot is calculated to be at 5.28°N, 25.3°W. The strike of whole-mantle, shear-wave velocity profile (see Figure 7) crossing the SW termination of the BSP (i.e., current location of the hotspot) is denoted by the solid black line that initiates from a white dot and ends at a black dot with green dots in between (the SW termination of the BSP is shown with an orange dot on this strike line). Outline of the Western African Craton after Begg et al. (2009) and surface projection of the large low-shear-wave velocity anomaly (LLSVP, stippled yellow line) in the lower mantle from Torsvik et al. (2006). Map source: <http://www.geomapapp.org>. b) Detailed bathymetric map of the working area compiled during Maria S. Merian cruise MSM70 (van der Zwan et al., 2018) and location of dredge sites for samples used in this study. The dredged sites from different segments of the BSP are denoted with different symbols that are also used on the geochemical diagrams: dark blue rectangles (Northern BSP), light blue diamonds (Central BSP) and green triangles (Southern BSP). Radiometric ages from Bertrand et al. (1993), Jones et al. (1991), Kharin et al. (1988) and Skolotnev et al. (2010). *Star denotes paleontological constraint age after Skolotnev et al. (2017). Basement isochrons (white lines) are shown at 10 Ma increments after Müller et al. (2016).

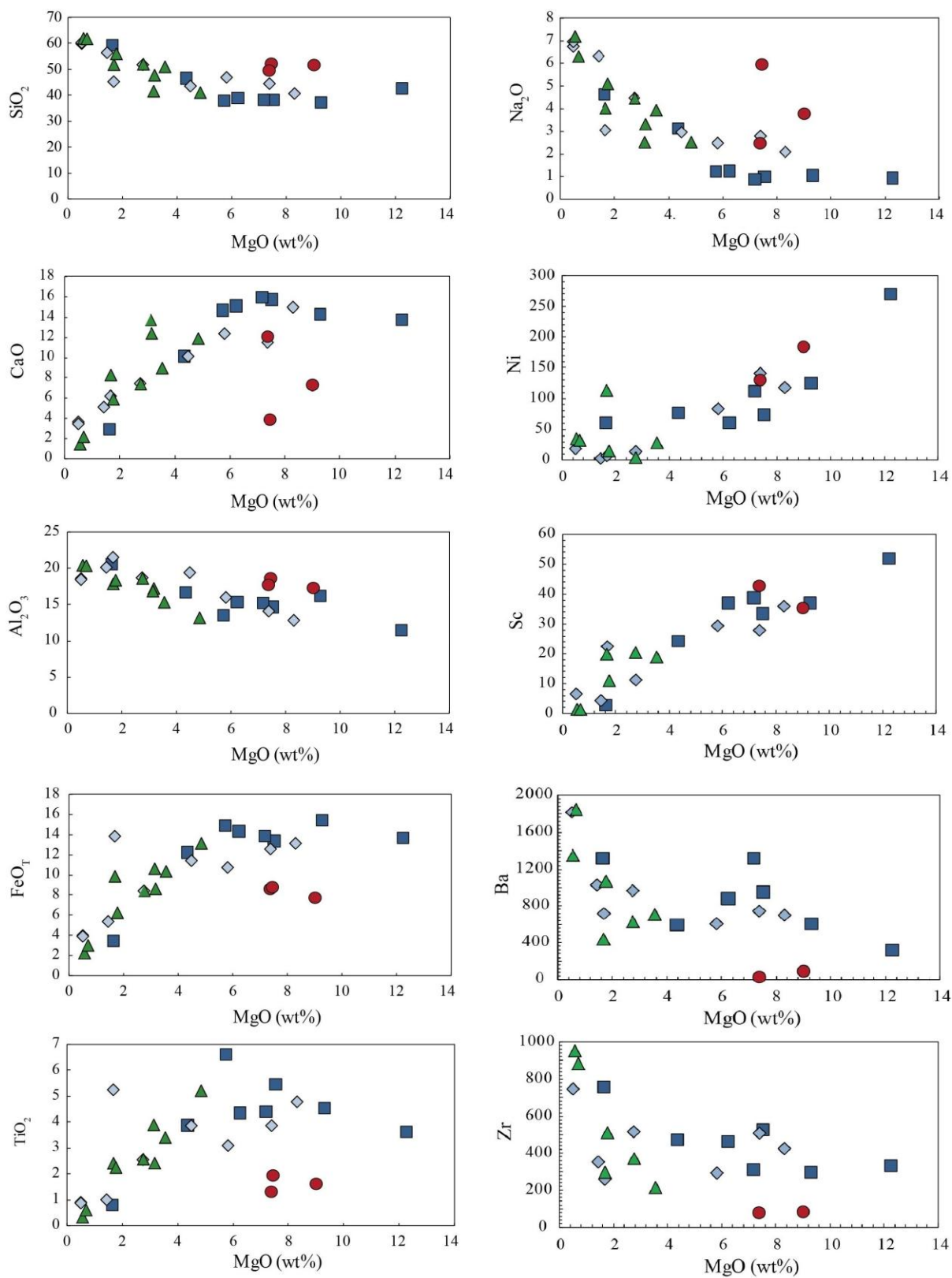


Figure 2. Variations of major elements (wt.% normalized to 100 % on a volatile-free basis) and trace elements (in ppm) versus MgO for samples from the BSP and the Cape Verde Ridge. See details in text (section 4.2).

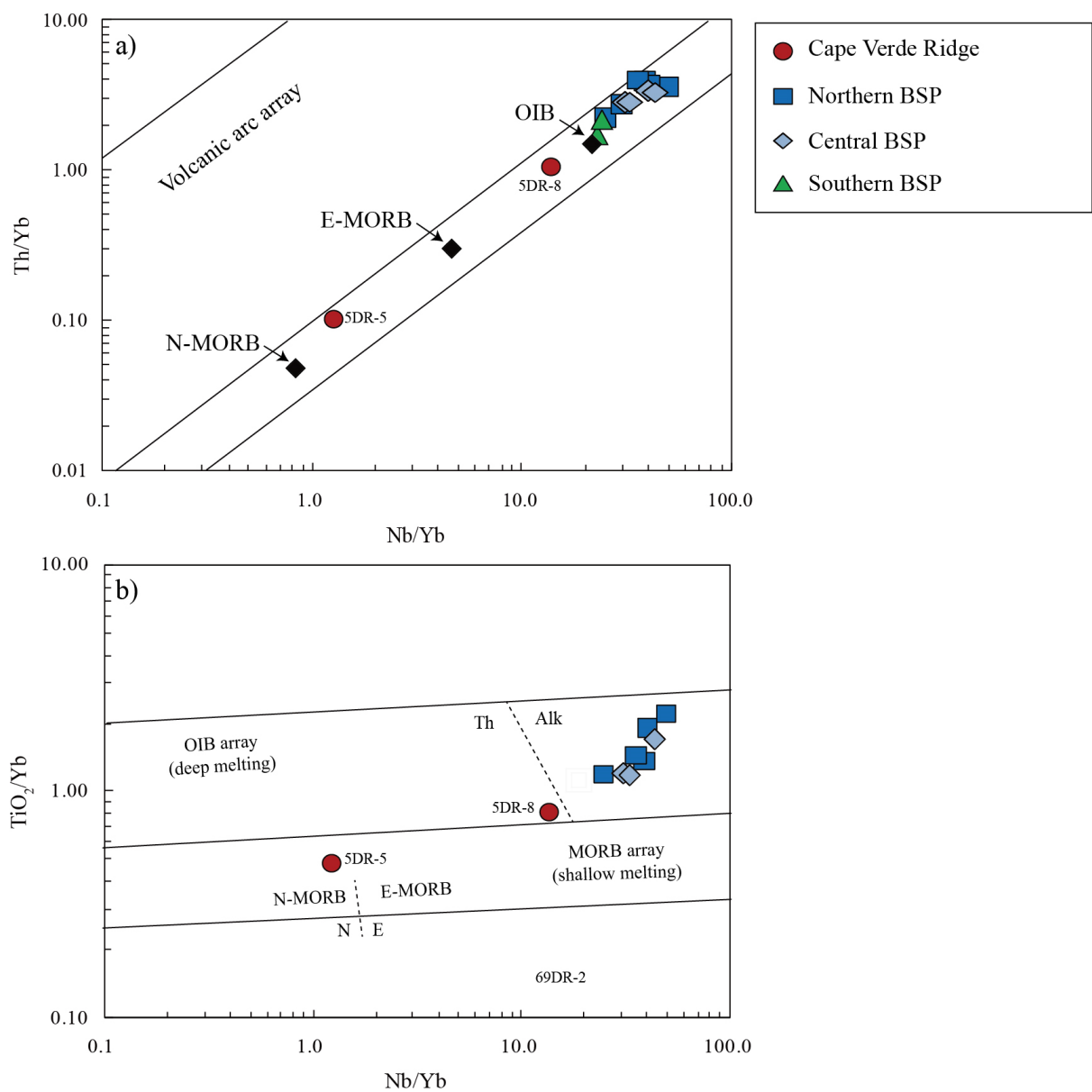


Figure 3. a) Nb/Yb vs. Th/Yb and b) Nb/Yb vs. TiO_2/Yb diagrams after (Pearce, 2008). Note that only samples with $\text{MgO} \geq 6$ wt% are shown in Figure 3b, due to decrease in TiO_2 as a result of Fe-Ti oxide fractionation (see text in section 4.2 or Figure 2).

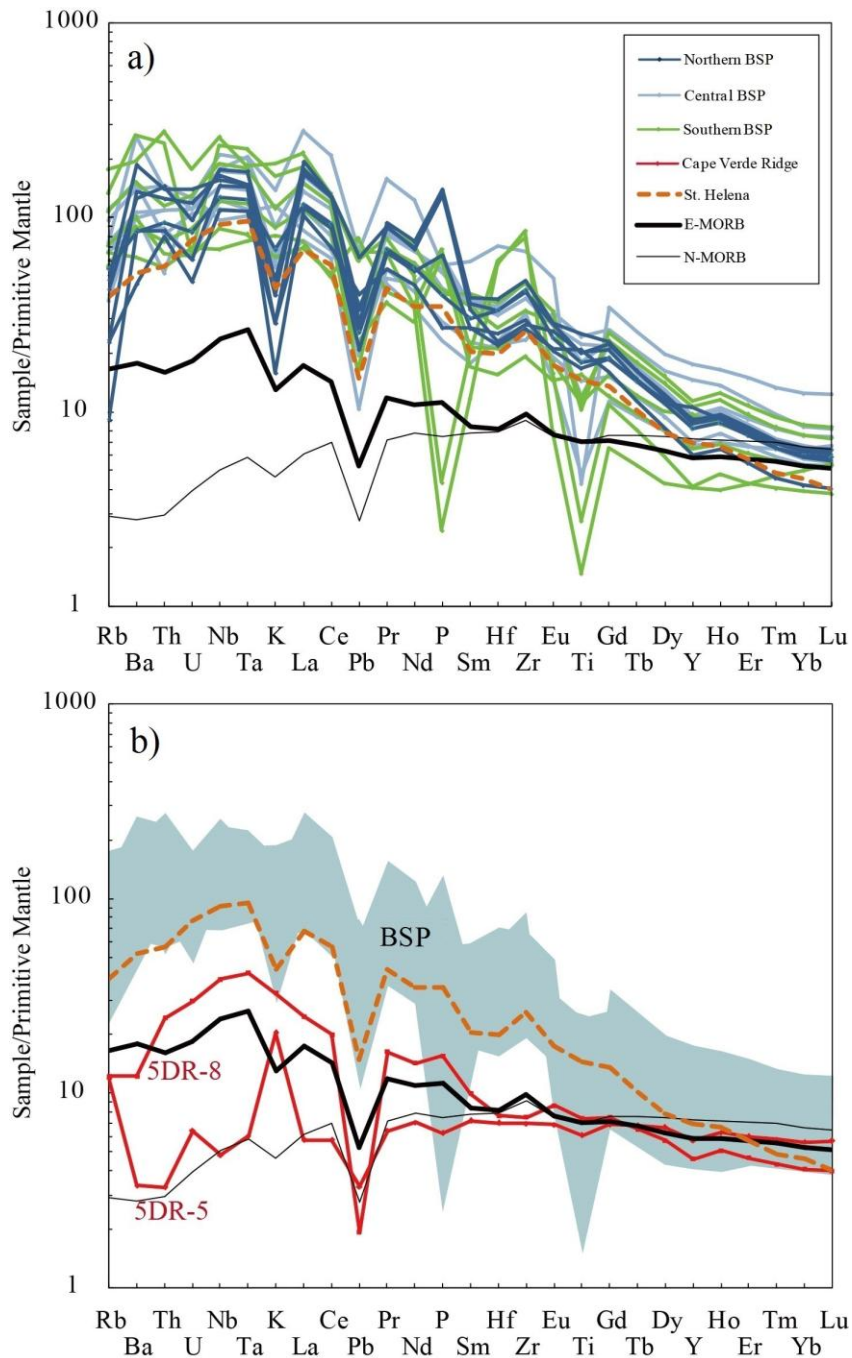


Figure 4. Multi-element diagrams of incompatible elements (normalized to primitive mantle after Sun and McDonough (1989)): a) BSP and b) Cape Verde Rise samples. The orange dotted lines in both diagrams represent the average HIMU pattern of lavas from St. Helena (Willbold and Stracke, 2006), whereas the thick and thin black lines represent the E- and N-MORB patterns, respectively (Gale et al., 2013). Grey area in 5b shows range of BSP composition. Unusual enrichment of particular fluid-mobile elements Rb and K in 5DR-5 could be caused by post-magmatic alteration.

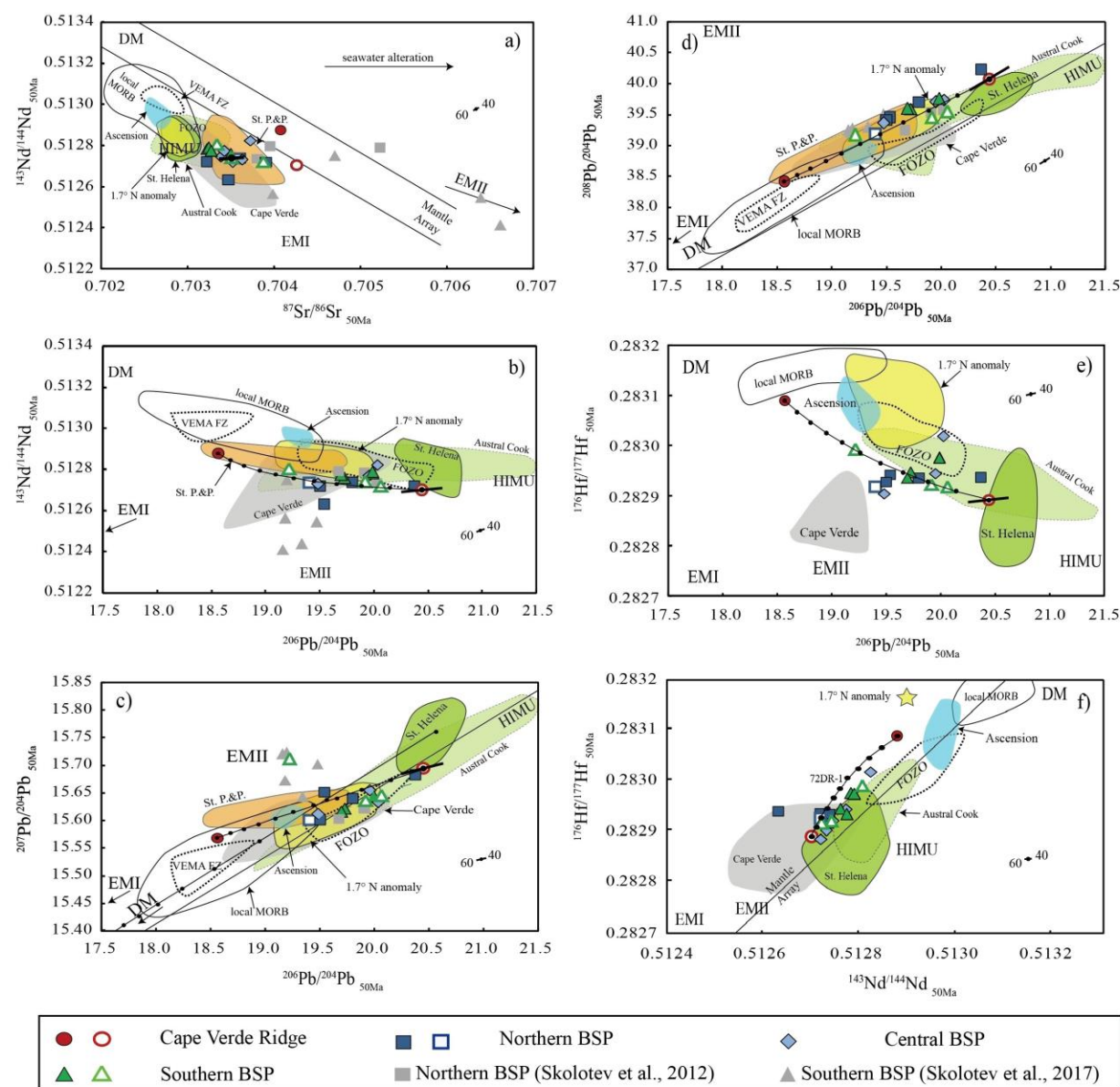


Figure 5. Initial Sr-Nd-Pb-Hf isotope ratios (see section 4.3 for details of applied age correction) of investigated lavas from BSP and Cape Verde Ridge shown in comparison to the Vema Fracture Zone (Dosso et al., 1993), St. Helena (Chaffey et al., 1989; Reisberg et al., 1993; Salters and White, 1998, Salters et al., 2011), Cook-Austral Islands (Hauri et al., 1993; Salters and White, 1998; Nakamura and Tatsumoto, 1988; Maury et al., 1994; Vidal et al., 1984; Chauvel et al., 1992; Woodhead, 1996; Duncan and McDougall, 1976; Schiano et al., 2001; Pfänder et al., 2007; Salters et al., 2011; Hanyu et al., 2011; Nebel et al., 2013; Hanyu et al., 2013), Cape Verde Islands (Barker et al., 2010; Doucelance et al., 2010; Holm et al., 2005; Martins et al., 2010; Mourão et al., 2012), Ascension Island (Paulick et al., 2010), the 1.7 N MAR anomaly (Schilling et al., 1994) and St. Peter and Paul Rocks (St. P.&P., Roden et al., 1984). Disturbance of the U-Pb system by seawater alteration cannot be ruled out for some samples from BSP and Cape Verde Ridge (see section 4.3), altered samples are therefore shown with open symbols and should be treated with caution. To evaluate the effect of age uncertainty on the initial isotopic compositions, the variation of an average BSP sample are shown in each isotope diagram with a 50 +/-10 Ma variation bar (small black dot in right corners of diagrams), using the following parent/daughter ratios: $^{87}\text{Rb}/^{85}\text{Sr} = 0.21$, $^{147}\text{Sm}/^{144}\text{Nd} = 0.11$, $^{238}\text{U}/^{204}\text{Pb} = 26.17$, $^{235}\text{U}/^{204}\text{Pb} = 0.19$, $^{232}\text{Th}/^{204}\text{Pb} = 119.17$, and $^{176}\text{Lu}/^{177}\text{Hf} = 0.0088$. The respective deviation of most BSP lavas is smaller than their symbol size in all isotope plots except for sample 55DR-4 in Figure 5a and sample 5DR-8 in Figure 5b-f for which individual +/-10 Ma variation bars are shown. Previously published isotope data of lavas (whole rock samples) from the BSP are also shown age corrected to 50 Ma with grey symbols (Skolotnev et al., 2012; Skolotnev et al., 2017, see these publications for trace element composition). The isotope ratios of the reference fields are all projected to 50 Ma using the following parent and daughter concentrations for their assumed source composition: HIMU-like (Rb = 0.568, Sr = 80.270, Sm = 2.677, Nd = 7.4549, U = 0.028, Th = 0.088, Pb = 0.092, Lu = 0.449, Hf = 1.781; Stracke et al., 2003) applied to samples from St. Helena, St. Peter and Paul Rocks and 1.7 N MAR anomaly; Primitive Mantle (Rb = 0.635, Sr = 21.1, Sm = 0.444, Nd = 1.354, U = 0.021, Th = 0.085 and Pb = 0.185, Lu = 0.074, Hf = 0.309; Sun and McDonough, 1989) for Cape Verde Archipelago; and MORB-like (Rb = 0.050, Sr = 7.664, Sm = 0.239, Nd = 0.581, U

=0.003, Th = 0.008 and Pb =0.018, Lu = 0.058, Hf = 0.157; Workman and Hart, 2005) for samples from
 local MORB and VEMA Fracture Zone. Mixing lines between depleted Cape Verde Ridge lava 5DR-5
 (believed to reflect local upper mantle) and enriched Cape Verde Ridge sample 5DR-8 (assumed to
 closest resemble the proposed BSP plume composition) are shown with 10% increments (black dots). DM,
 EMI, EMII and HIMU isotope end member compositions are from Zindler and Hart (1986). Stippled field
 for FOZO is from Stracke et al. (2005).

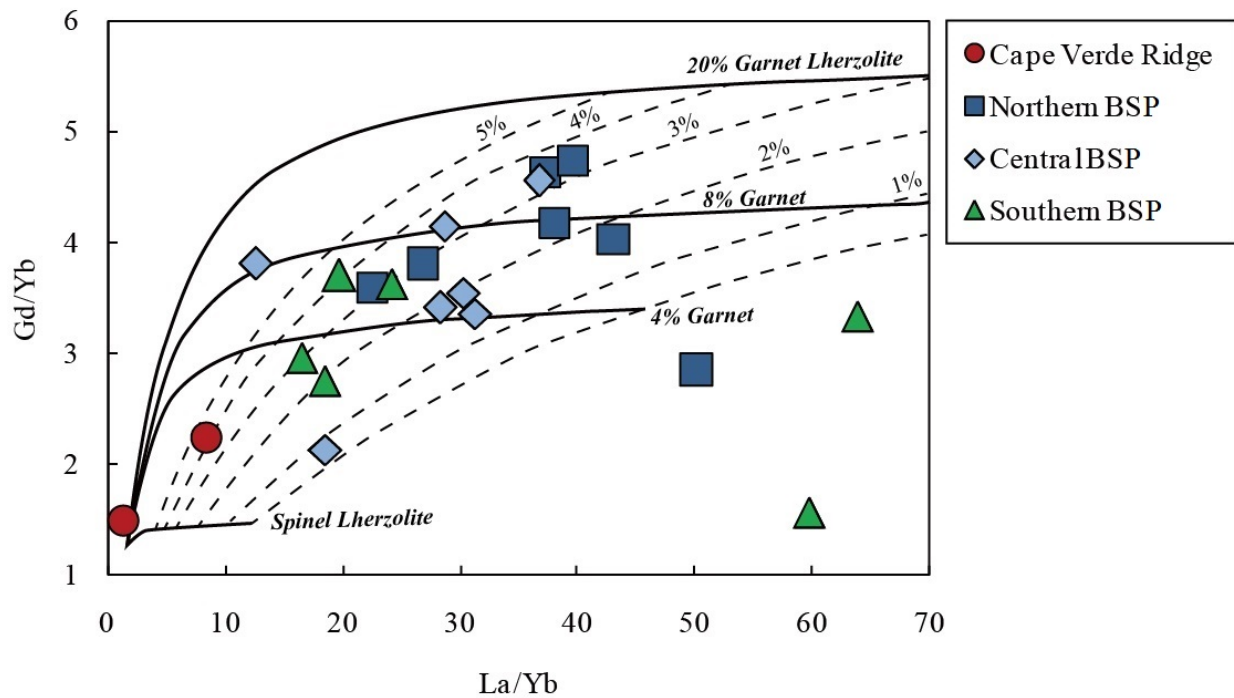
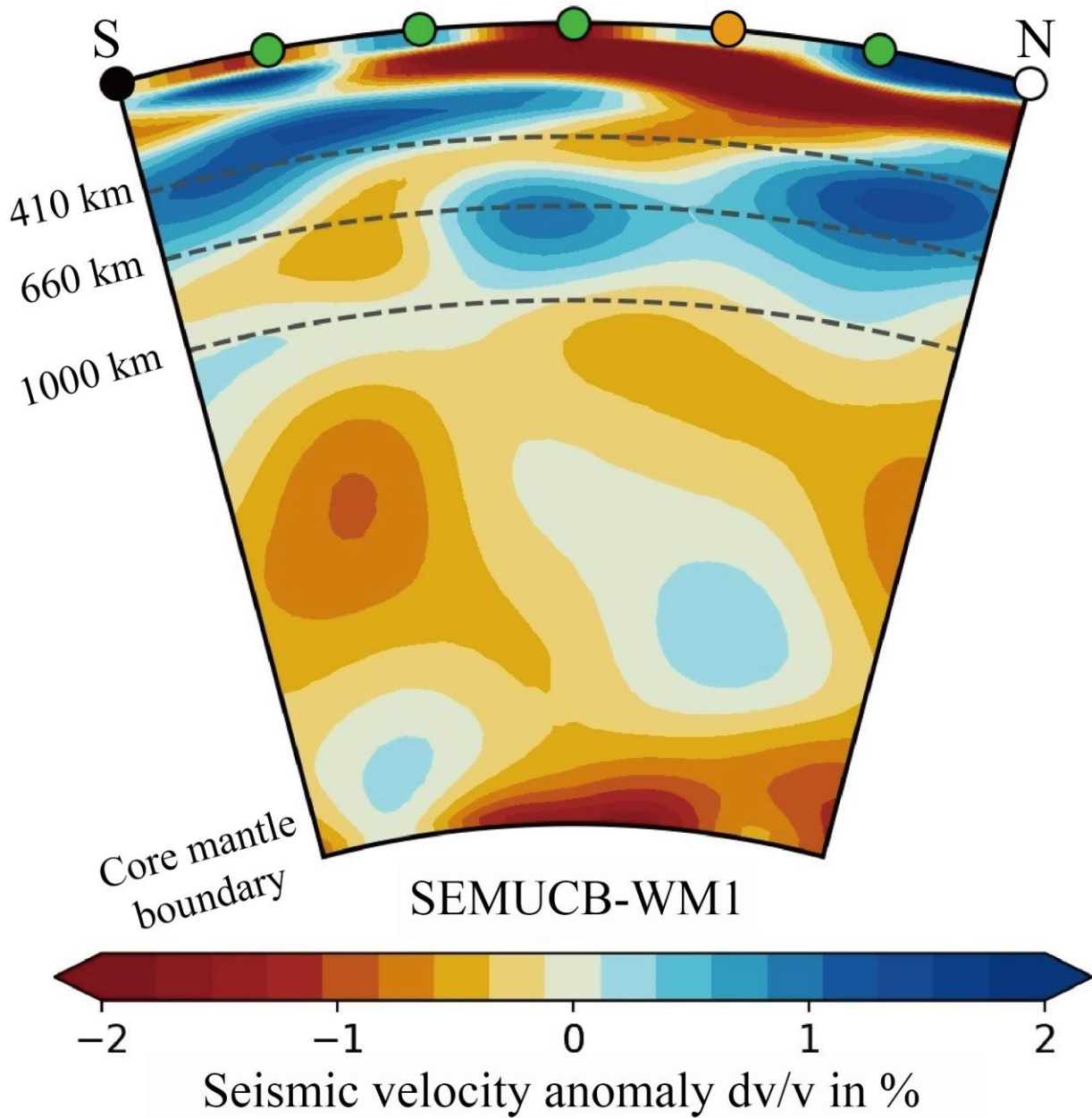


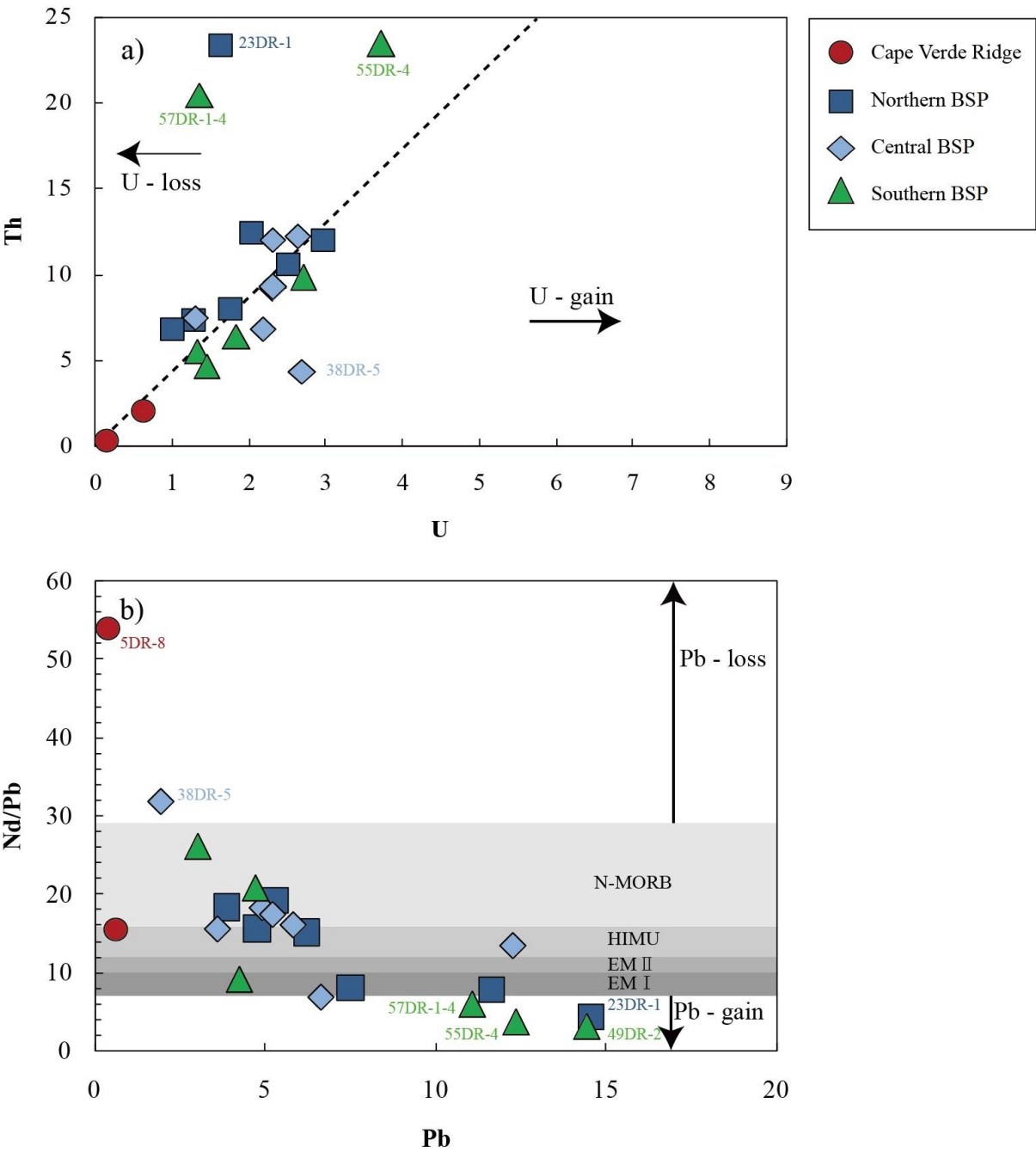
Figure 6. La/Yb vs Gd/Yb diagram of volcanic samples from the BSP and Cape Verde Ridge together
 with melting models from Yokoyama et al. (2007), reflecting variations of garnet in the source (solid lines)
 and different degrees of partial melting (dashed lines).



1184

1185 Figure 7. Whole-mantle depth profile of relative shear-velocity crossing the SW termination of the BSP
 1186 (i.e., the calculated current position of the hotspot, shown as an orange dot). Strike of this profile is shown
 1187 in Figure 1a. Sketch is drawn based on the whole-mantle shear-wave velocity model of SEMUCB-WM1
 1188 from French and Romanowicz (2014, 2015) and created with the webpage:
 1189 <https://www.earth.ox.ac.uk/~smachine/cgi/index.php>. The SW termination of the BSP is underlain by a
 1190 slow shear-velocity anomaly.

1191



1192

1193 Figure A1. (a) U vs. Th and (b) Pb vs. Nd/Pb for samples that were selected for isotope measurements to
1194 evaluate the effect of seawater alteration/metamorphism on the Th-U-Pb isotope system.